Aus dem Walter-Brendel-Zentrum für Experimentelle Medizin

der Ludwig-Maximilians-Universität München

Vorstand: Prof. Dr. U. Pohl

Intravital Multiphoton Microscopy Analysis of Spatial Relationships in Murine Skull Bone Marrow

Dissertation

zum Erwerb des Doktorgrades der Medizin

an der Medizinischen Fakultät

der Ludwig-Maximilians-Universität zu München

vorgelegt von

Katharina Engelke

aus

Göttingen

2009

Mit Genehmigung der Medizinischen Fakultät

der Universität München

1. Berichterstatter:	Prof. Dr. F. Krombach
2. Berichterstatter:	Prof. Dr. Marc Dellian
Mitberichterstatter:	Prof. Dr. Monika Führer
	Prof. Dr. Jochen Herms
Mitbetreuung durch den promovierten Mitarbeiter:	-
Dekan:	Prof. Dr. med. Dr. h.c. M. Reiser, FACR, FRCR
Tag der mündlichen Prüfung:	30.07.2009

Index of Content

LIST OF FIGURES **1-5**

LIST OF TABLES **1-7**

ABBREVIATIONS **1-8**

1 INTRODUCTION **1-9**

1.1 BONE MARROW 1-9

1.1.1 Bone Marrow Function 1-9

1.1.2 Bone Marrow Configuration 1-10

1.1.3 Previous Intravital Microscopy Studies in the Bone Marrow 1-12

1.2 MULTIPHOTON MICROSCOPY 1-15

1.2.1 History, Theory and Physics of Multiphoton Microscopy 1-15

1.2.2 Previous Multiphoton Microscopy Studies 1-21

2 AIMS OF THE STUDY **2-24**

3 MATERIALS AND METHODS **3-26**

3.1 EXPERIMENTAL DESIGN 3-26

3.1.1 Place of the Study 3-26

3.1.2 Components 3-26

3.1.3 Preparation of the Animal 3-35

3.1.4 Intravital Microscopy Experiments 3-37

3.2 IMAGE PROCESSING AND ANALYSIS 3-44

3.2.1 Quantification of Bone Marrow 3-44

3.2.2 Adoptive Transfer Experiments 3-50

3.2.3 Vessel Diameter Measurements 3-51

3.2.4 3D Reconstruction from Processed Image Stacks 3-52

3.3 STATISTICS 3-52

3.3.1 Bone Marrow Quantification 3-52

3.3.2 Adoptive Transfer Experiments 3-52

4 RESULTS 4-54

4.1 ANATOMY AND MORPHOLOGY OF THE BONE MARROW 4-54

4.2 QUANTIFICATION OF BONE MARROW COMPARTMENTS 4-56

4.3 ADOPTIVE TRANSFER EXPERIMENTS 4-61

5 DISCUSSION 5-67

5.1 MULTIPHOTON IMAGING IN THE BONE MARROW ORGAN 5-67

5.2 EXPERIMENTAL DESIGN OF THE STUDY 5-74

5.3 IMAGE PROCESSING AND ANALYSIS 5-79

5.4 SPATIAL RELATIONSHIPS IN THE BONE MARROW 5-82

5.5 SUBCOMPARTMENTALIZATION OF THE BONE MARROW 5-84

6 SUMMARY 6-87

7 ZUSAMMENFASSUNG 7-88

8 REFERENCES 8-90

9 DANKSAGUNG 9-102

10 CURRICULUM VITAE 10-103

List of Figures

Figure 1. Organization of BM microvasculature in murine skull BM 1-14

Figure 2. CLSM in scattering media 1-16

Figure 3. Principle of multiphoton excitation compared to confocal excitation... 1-18

Figure 4. MPM in scattering media 1-19

Figure 5. Phenotype of T_{CM} 3-30

Figure 6. Phenotype of total splenocytes 3-31

Figure 7. MACS purification of naïve B-cells by negative selection 3-33

Figure 8. Phenotype of enriched naïve B-cells 3-34

Figure 9. Animal preparation and immobilization technique of the mouse 3-36

Figure 10. Configuration of the MPM system 3-38

Figure 11. Image acquisition during the experiment 3-41

Figure 12. “Montage” of the BM region investigated during one experiment 3-42

Figure 13. Additional Image Acquisition in Adoptive Transfer Experiments 3-44

Figure 14. Image processing technique in Adobe Photoshop 3-47

Figure 15. Comparison of a raw data section with its corresponding processed section 3-48

Figure 16. Measurement performance by VoxBlast 3-49

Figure 17. Image analysis in adoptive transfer experiments 3-51

Figure 18. Arrangement of microvascular segments in the frontoparietal region of skull BM 4-55

Figure 19. IV at different depth below skull surface 4-56

Figure 20. Spatial relationships of BM compartments in different microvascular segments 4-57

Figure 21. 3D reconstruction of an IV 4-61

Figure 22. T_{CM} home to the BM compartment 4-62

Figure 23. Analysis of T_{CM} homing 4-64

Figure 24. Analysis of naïve B-cell homing 4-66

Figure 25. Comparison of MPM and CLSM in XZ images of a CV 5-69

Figure 26. Comparison MPM and CLSM in XY images of a CV 5-69

Figure 27. Penetration depth in MPM 5-71

Figure 28. Fluorescence distribution in a BM cavity 5-77

List of Tables

Table 1. Diameters and ratios of intravascular to extravascular space for different microvascular segments..... 4-58

Table 2. Dimensions of BM microvessels by Mazo *et. al.* 4-58

Abbreviations

BM	bone marrow
T_{CM}	CD8+ central memory like T-cells
3D	three-dimensional
2D	two-dimensional
IVM	intravital microscopy
CV	collecting venule
IV	intermediate venule
PSV	postsinusoidal venule
CN	capillary network
S	sinusoids
MPM	multiphoton microscopy
UV	ultra-violet
CLSM	confocal laser scanning microscopy
FITC	fluorescein isothiocyanate
FBS	fetal bovine serum
PBS	phosphate-buffered saline
ACK	ammonium chloride
IR	infra-red
AOI	area of interest
SD	standard deviation
MRI	magnetic resonance imaging

1 Introduction

1.1 Bone Marrow

1.1.1 Bone Marrow Function

The bone marrow (BM) is the key primary lymphoid organ of the body. It is the principal site of hematopoiesis of lymphoid and myeloid cell lineages and has a pivotal role in generating erythrocytes and thrombocytes. In particular, the BM is the major site of postnatal B-cell development (Osmond, 1986; Rajewsky, 1996). In addition, the BM can assume the function of a secondary lymphoid organ; it has been shown that naïve T-cells can differentiate into effector T-cells in the BM (Tripp et al., 1997; Feuerer et al., 2003). Although anatomically distinct, the BM shares some similarities with bona fide secondary lymphoid organs, such as B-cell like follicles (Horny et al., 1989) and areas that are enriched for T-cells (Schirrmacher et al., 2003). Indeed, there is evidence that the BM takes part in primary and secondary T-cell responses to antigen. It has been shown that naïve and memory T-cells are situated in the BM (Di Rosa and Santoni, 2002) and both cell subsets home to the BM (Berlin-Rufenach et al., 1999; Di Rosa and Santoni, 2003; Mazo et al., 2005). Recent investigations demonstrate that antigen-bearing dendritic cells home to the BM where they interact with central memory T-cells (T_{CM}) and trigger recall responses to model antigens (Cavanagh et al., 2005). Furthermore, the BM is considerably involved in humoral immunity: it harbors antibody-producing plasma cells and memory B-cells, which can be recruited from the blood (Manz et al., 1997; Paramithiotis and Cooper, 1997; Hallek et al., 1998; Slifka et al., 1998; Ellyard et al., 2004). The many different BM cell populations are

believed to have a well-defined spatial organization depending on their state of development (Lord et al., 1975). Immature and most primitive cells are thought to localize close to the endosteum and subendosteal region of the BM cavities (Nilsson et al., 2001; Calvi et al., 2003; Zhang et al., 2003), whereas more mature blood cells rather reside preferentially in the central area after migration from the outer parts of the cavity during development (Lord et al., 1975; Hermans et al., 1989). It has been shown, that this migration within BM cavities requires stroma cells and certain chemoattractants (Tokoyoda et al., 2004).

We have only recently begun to dissect the many complex steps that govern lymphocyte maturation and differentiation in the BM and our understanding of the BM´s role in adaptive immunity is also incomplete. This study will provide a spatial microanatomic view on murine skull BM.

1.1.2 Bone Marrow Configuration

The BM is located in the medullary canals of long bones and cavities of cancellous bones. Structurally, the BM organ can be divided into two compartments: an extravascular compartment, of mostly hematopoietic tissue, and an intravascular compartment consisting primarily of venous blood vessels (Weiss, 1965). The extravascular compartment consists of a connective tissue, a complex vasculature, among other formed by sinusoidal capillaries, and the hematopoietic compartment itself, united to a sophisticated three-dimensional (3D) network. This complex 3D architecture of the BM is difficult to reveal in situ and at the single-cell level. First, the investigation is complicated by the anatomic inaccessibility of the BM. Second, traditional imaging techniques were limited to the derivation of two-

dimensional (2D) information.

There have been previous attempts to investigate certain spatial relationships of the BM to address different clinical questions. For example, Naito *et al.* explored the basic architecture of the BM by examining sectioned biopsies of human iliac bones and submitting photographs of stained sections to computer-assisted 3D reconstruction (Naito et al., 1992). Looking at osteomyelofibrosis in humans, Kvasnicka *et al.* also used sectioned human bone biopsies in combination with a software for 3D reconstruction to gain insights into the spatial arrangement of certain BM structures in this disease (Kvasnicka et al., 1994). Two other studies concentrated on the spatial distribution of adipose tissue compared to active marrow using nuclear magnetic resonance tomography of human femoral head biopsies (Bolch et al., 2002; Patton et al., 2002). The latter two studies provided 3D information of the BM. However, sectioned biopsies were examined. Consequently, the 3D information is based upon the reconstruction of 2D material. Moreover, the generation and processing of biopsies could potentially influence the microanatomic architecture, e.g. by causing tissue shrinkage and distortion due to lack of blood flow. Therefore, it is uncertain whether these studies yield an exact 3D reflection of the true physiological state. In addition, these studies were largely descriptive and did not produce rigorous data of BM architecture.

Pannerale *et al.* focused on the organization of the BM microcirculation in flat bones and tried to maintain the total microcirculation in the bone in a rat model. Corrosion cast material was prepared (the blood was substituted by a resin material, which then polymerized) and scanning electron microscopy studies on histological sections of this material were performed (Pannerale et al., 1997). Despite the attempt to preserve the microcirculation as completely as possible, the

utilization of histological preparations could again result in distortions, and this technique cannot reveal extravascular features.

The first step to a truly quantitative spatial analysis of the BM microenvironment is to view this microenvironment *in vivo* within intact bone. There have been previous attempts at performing intravital microscopy (IVM) studies on the BM. These studies are briefly outlined below.

1.1.3 Previous Intravital Microscopy Studies in the Bone Marrow

IVM is a technique of capturing microscopic images directly from a living animal. This technique has already provided much insight into the anatomy of lymphoid organs and the function of various lymphoid microenvironments and events involving subsets of lymphocytes (Smedegard et al., 1985; Hoffmann et al., 1995; von Andrian, 1996; Warnock et al., 1998; Becker et al., 2000; Grayson et al., 2001; Piccio et al., 2002; Rosenbaum et al., 2002; Carballido et al., 2003; Laudanna and Constantin, 2003; Sikora et al., 2003; Mempel et al., 2004a; Germain et al., 2006; Celli et al., 2008). Recent advances combine IVM with multiphoton technology to approach the immunology field; those are cited later in the introduction. About four decades ago it became possible for the first time to conduct IVM in the BM, which is embedded in compact bone, and therefore not directly accessible. Branemark developed a model to look at the BM microcirculation in rabbit fibula by grinding down the compact bone to a relative thin layer providing a transparent bone window (Branemark, 1959). This study was the first to describe the pattern of the capillary network in the BM microenvironment and its hemodynamic parameters. Two years later, a similar *in situ* model was described in rabbits aiming at the

investigation of events occurring during BM regeneration (Kinosita and Ohno, 1960). In this case, a glass chamber was inserted into the tibia or femur and the regenerating tissue on the glass surface of the chamber was viewed. McCuskey *et al.* designed a chamber to allow long-term observation of BM in the rabbit tibia and confirmed results on the microvascular system already obtained by other groups (McCuskey et al., 1971). Although these studies had overcome the relatively inaccessible nature of the BM, these early IVM techniques necessitated undesirable trauma to the bone, its endosteum and the marrow itself. Consequently, inflammation, induced hemorrhage and reactions of the tissue to implants, such as metal or glass, could potentially alter the integrity and function of the BM impairing true insight into its physiologic state, particularly with regard to immunological events. Moreover, while these studies presented the first comprehensive analysis of some structural features of living BM, including its microvascular system, the 3D architecture and spatial relationships were not examined due to technical restrictions of available microscopy techniques.

In 1998, the von Andrian lab described an IVM technique that allowed direct observation and analysis of physiologically perfused BM microvessels in a mouse model using conventional epifluorescence video microscopy (Mazo et al., 1998). This technique takes advantage of the anatomy of the flat bones forming the calvarium of the mouse skull. In the frontoparietal part imaging of untouched BM is feasible through a thin layer of bone without requiring any surgical manipulation of the bone itself. Our group characterized the anatomy of the BM microvasculature of this frontoparietal part of the skull (Figure 1) and analyzed hemodynamic parameters. In Figure 1 the microvascular structure observed by epifluorescence video microscopy is described: The BM collecting venule (CV) (1) collects blood

from intermediate venules (IV) (5) and laterally located postsinusoidal venules (PSV) (4) and drains almost perpendicularly into the superior sagittal sinus (2). One or more PSV (4) receive blood from medially located sinusoids (S) (3) and run to the CV (1). S are in close relation to each other and form a sinusoidal network. Not only the microvasculature but also adhesion events of hematopoietic progenitor cells in different situations were examined with the use of the model described above (Mazo et al., 1998; Mazo and Von Andrian, 1999; Mazo et al., 2002; Cavanagh et al., 2005; Mazo et al., 2005).

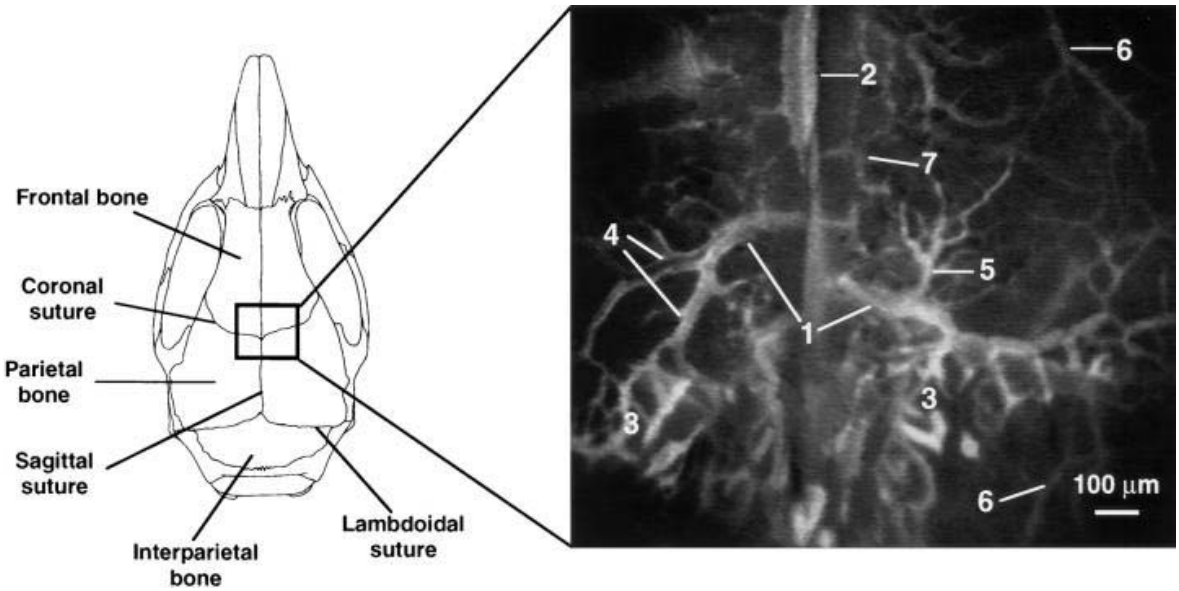

Figure 1. Organization of BM microvasculature in murine skull BM

Left: schematic drawing of dorsal mouse skull. Flat bones and sutures are schematically shown. The rectangle indicates the area showing the typical BM microvasculature Right: The superior sagittal sinus (2) collects blood from the BM CV (1), which drains almost perpendicularly into it. The BM CV (1) receives blood from a network of laterally located S (3), from BM IV (5) and from a BM PSV (4), which serves as a conduct between medially located S and the CV. Bone vessels (6) in this region are not in contact with the BM microenvironment. Figure by Mazo *et al.* (Mazo et al., 1998)

In this study, we have adapted the skull BM IVM model to make use of a relatively new imaging tool, multiphoton microscopy (MPM). The second part of the introduction will further elucidate and discuss this technique.

1.2 Multiphoton Microscopy

1.2.1 History, Theory and Physics of Multiphoton Microscopy

Multiphoton excitation has become a novel optical imaging tool for fluorescence microscopy in various fields. In order to clarify the advantages of this technique the history and basics of microscopy are summarized in the next paragraph following the structure of a review by Denk *et al.* (Denk and Svoboda, 1997): The broad application of intravital fluorescence microscopy relies on the capability to investigate living tissue at relatively high resolution. This strategy must cope with two major challenges, the potential of severe photodamage and bleaching caused by ultra-violet (UV) and short wavelength visible light and the limitation of 3D imaging in thick samples due to degradation of resolution and contrast with increasing tissue depth, when high resolution imaging eventually becomes impossible. This effect is based on the relatively short wavelength of light and resulting light scattering, due to refractive index mismatches in heterogeneous tissues. The invention of one-photon confocal laser scanning microscopy (CLSM) by Minski in 1961 greatly improved depth discrimination and spatial resolution (Minski, 1961). Generally, in laser scanning microscopy, a laser beam of a certain wavelength, excitation light, is focused to a small diameter and is raster-scanned through the specimen. Fluorescently labeled details of the specimen are excited and emit photons, emission light, that is collected and forms the image. The

principle of CLSM is portrayed in figure 2. The entire specimen is excited by excitation photons, because a considerable amount of photons are scattered in the sample. Resulting signal photons, emission light, is collected through the same optics and caught by a detector, after passing a pinhole, which prevents the collection of scattered and out-of-focus light/photons (Figure 2).

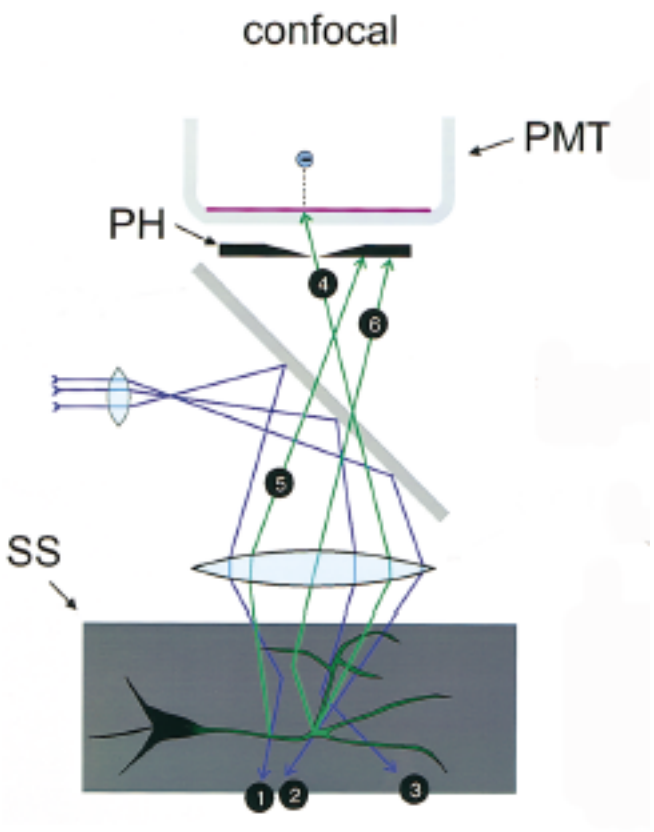

Figure 2. CLSM in scattering media

Many excitation photons (blue lines) are scattered (1 and 3) because of their short wavelength. Just a small fraction of the excitation light reaches the focal plane (2). The total sample (SS) is affected by excitation (green region of the specimen). Generated fluorescent photons (green lines) from out of focus locations (5) and those being scattered on their way back (6) are rejected by a pinhole (PH). Only unscattered photons (4) generated at the focus spot reach the photomultiplier detector (PMT) and form the image. Figure by Denk *et al.* (Denk and Svoboda, 1997)

In CLSM absorption of excitation light takes place throughout the specimen, whereas emission light forming the image is solely collected from a thin slice around the focal plane. This effect leads to a major problem, especially when investigating living tissue. Absorption of light by the fluorophore entails photodynamic damage (phototoxicity) to the specimen. Additionally, photobleaching - photodestruction of a fluorophore - results in fading of signal and therefore limits the observation. Only light that was not scattered during its path through the tissue contributes to the signal and image, while scattered light, often the majority, is rejected by the pinhole in front of the detector. To compensate for this signal loss it is necessary to increase light illumination, especially at greater imaging depth, leading to exacerbation of photodamage and photobleaching.

These disadvantages are solved or at least reduced when using MPM. Multiphoton excitation was first predicted in 1931 by Maria Göppert-Mayer in her doctoral thesis (Göppert-Mayer, 1931). Its application to laser scanning microscopy was introduced by Webb´s group at Cornell University and since then has found application among many scientific disciplines (Denk et al., 1990). The key difference between confocal and MPM lies in the excitation light: In CLSM a fluorescent molecule becomes excited by the energy of one single photon of a relatively short wavelength (i.e. relatively high energy), whereas in multiphoton excitation, a much longer wavelength excitation (=lower energy) source is used. To achieve fluorescence, two (or more) low energy photons must combine their energy to excite the specimen by simultaneous absorption of these photons by the fluorophore (Figure 3) (Denk and Svoboda, 1997).

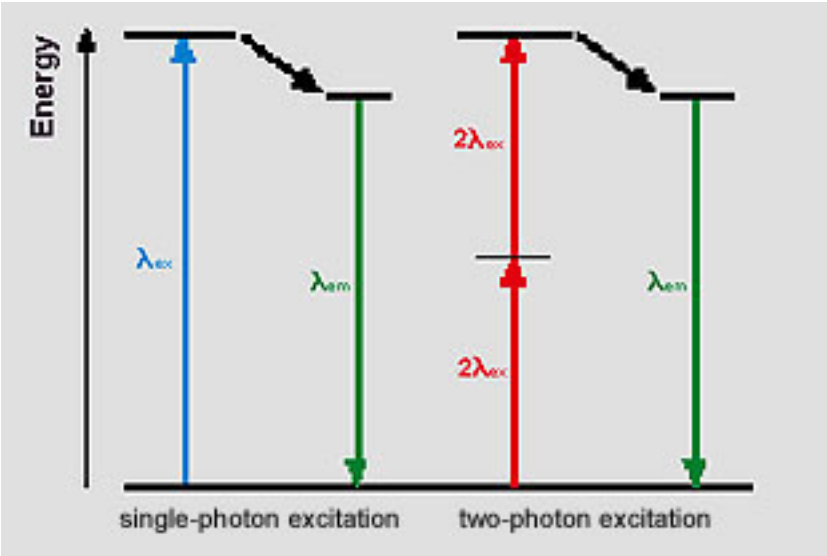

Figure 3. Principle of multiphoton excitation compared to confocal excitation

(Left) In CLSM (and other conventional fluorescence modalities) one photon of a certain wavelength (λ_{ex}, blue arrow) is used to excite a fluorescent molecule resulting in an emission photon (λ_{em}, green arrow). (Right) In MPM two (or more) photons at double that wavelength ($2\lambda_{ex}$, red arrows) act simultaneously to gain an equal signal of fluorescence (λ_{em}, green arrow). Figure from BioRad Manual (Biorad Laboratories, Hemel Hempstead, UK)

This is made possible by a very high local instantaneous intensity provided by the tight focusing of the excitation beam through an objective in a laser scanning microscope combined with the temporal concentration of photons in a femtosecond pulsed laser. A colliding-pulse, mode-locked laser, that produces a stream of pulses with a pulse duration in the femtosecond range at a high repetition rate, makes it possible that a dye molecule can absorb two long-wavelength photons simultaneously, using the combined energy of both photons to reach its excited state (Denk et al., 1990; Denk and Svoboda, 1997). Otherwise, concentration and combination of two photons fails, equally excitation of the fluorophore. All technical issues are discussed in detail by Denk *et al*. (Denk et al.,

1990; Denk et al., 1995). The principle of a multiphoton setup and imaging of a specimen by MPM are illustrated in figure 4. Only those parts of the specimen that lie in the focal plane are excited by the combined energy of two low-energy photons. Other parts of the specimen escape a photoreaction. All emission photons are detected and contribute to the image, no pinhole is needed to block scattered and out-of-focus light (Denk and Svoboda, 1997) (Figure 4).

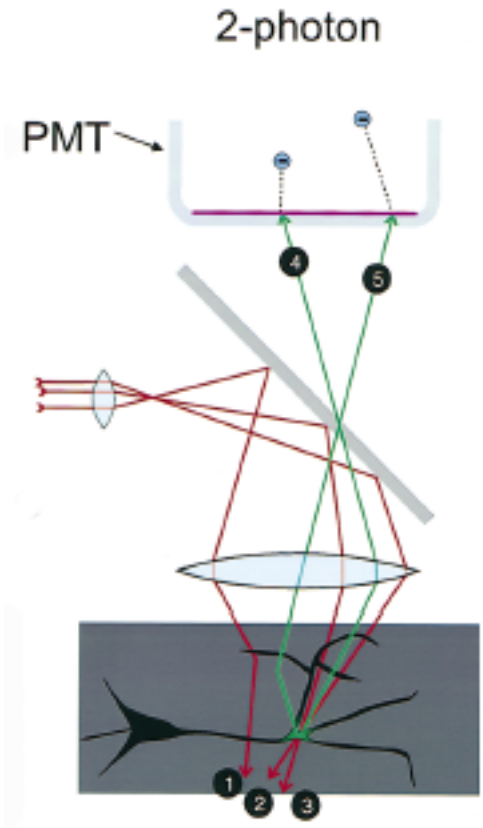

Figure 4. MPM in scattering media

A larger number of excitation photons (red lines) reach the focus spot (2 and 3). Solely in the focal plane the specimen gets excited by the combined energy of two unscattered photons (green area of the specimen). Some low-energy excitation photons are still scattered (1), but do not cause a photoreaction. Generated emission photons (green lines), unscattered (4) and scattered (5), contribute to the image, after being detected by the photomultiplier detector (PMT). Figure by Denk *et al.* (Denk and Svoboda, 1997)

In contrast to using descanned detectors (emission light returns along the same path as the excitation light to be detected) it is possible in MPM to use non-descanned or direct detectors. The emitted light is collected by an external detector directly from the specimen, without passing through the objective lens again. The non-descanned path enables the collection of more scattered photons, therefore collection efficiency is increased (Le Grand et al., 2008).

The fundamental physics of MPM are summarized and described in more detail by Nakamura (Nakamura, 1999).

From the physical principle of multiphoton excitation, one can conclude that this technique has many advantages compared to CLSM. First, multiphoton excitation offers intrinsic optical sectioning properties, since fluorescence is generated solely in the vicinity of the focal plane, whereas in CLSM and other single-photon excitation techniques all tissue elements in the beam pathway get excited. Second, this specially restricted generation of fluorescence results in greatly reduced photodamage and -bleaching. Photodamage is further minimized in MPM by using a lower energy wavelength, which makes this technique even more suitable for live imaging. The predicted decrease in photodamage and -bleaching when using MPM has been intensively studied (Patterson and Piston, 2000; Hopt and Neher, 2001). Squirrell *et al.* reported that multiphoton imaging allows long-term fluorescence observations in living mammalian embryo, whereas using confocal excitation viability is impaired after a short period of time (Squirrell et al., 1999). Third, deeper tissue penetration can be achieved since light with a longer excitation wavelength is scattered less. Another advantage of MPM is the increased signal strength because all fluorescence photons, even when scattered, constitute a useful signal and contribute to the image. Additionally, multiphoton

excitation offers multifluorophore excitation, where excitation light at a single wavelength simultaneously induces the visible fluorescence of a wide range of fluorophores. A basic parameter of fluorescence is the fluorescence excitation cross section. Although absorption spectra for fluorophores using onephoton excitation are broadly documented, little is known about the absorption spectra in twophoton excitation. Spectral features are yet not fully understood. Since it is difficult to predict these spectra, measurement reports of twophoton fluorescence excitation cross sections show convenient absorption spectra of frequently used fluorophores. These reports show that fluorescence microscopy based on twophoton excitation works well with a broad range of fluorophores and available laser sources (Xu and Webb, 1996; Xu et al., 1996).

In summary, MPM is a sophisticated tool with many advantages over other microscopy techniques that enables high resolution optical sectioning and allows investigations especially within deep living tissue, while the native physiological state can be preserved.

1.2.2 Previous Multiphoton Microscopy Studies

MPM has been broadly applied to conduct fluorescence imaging experiments in biological research. In the literature the use and advantages of MPM in various fields are comprehensively discussed and reviewed (Denk and Svoboda, 1997; König, 2000; Cahalan et al., 2002; Helmchen and Denk, 2002; Wei et al., 2003; Mempel et al., 2004b; Sumen et al., 2004; Germain, 2005; Germain et al., 2005; Halin et al., 2005; Tozer et al., 2005; Cahalan and Parker, 2006; Garaschuk et al., 2006; Germain et al., 2006; Mora and von Andrian, 2006; Bajenoff and Germain,

2007; Celli and Bousso, 2007; Cavanagh and Weninger, 2008; Germain et al., 2008). In this paragraph, some applications of multiphoton excitation in combination with IVM in various fields are summarized focusing on *in vivo* studies and recent investigations in the immunology field.

Neuroscientists have extensively used MPM because of its unique capability to study a microenvironment deep within a tissue, such as the brain, leaving network structures intact. For example, *in vivo* studies of “Alzheimer disease”, stroke pathology, placticity of dendritic spines, dendritic calcium dynamics, synaptic learning and the olfactory bulb can be found in the literature (Svoboda et al., 1997; Helmchen et al., 1999; Lendvai et al., 2000; Christie et al., 2001; Chaigneau et al., 2003; Garcia-Alloza et al., 2006; Garcia-Alloza et al., 2007; Gobel and Helmchen, 2007; Harvey and Svoboda, 2007; Prada et al., 2007; Harvey et al., 2008; Meyer-Luehmann et al., 2008; Murphy et al., 2008). MPM has also been applied in the field of tumor physiology (Brown et al., 2001; Wolf et al., 2003; Kedrin et al., 2007; Wang et al., 2007; Lai Guan Ng, 2008) and in the investigation of dynamics of tumor angiogenesis and vascular function (Tozer et al., 2005). Zinselmeyer *et al.* introduced a model to study the cellular basis of inflammation by MPM (Zinselmeyer et al., 2008). Recently, the potential of investigating the physiology of the kidney by MPM was described (Carrasco and Batista, 2007).

In addition, immunologists have recently started to exploit the advantages of this technique to obtain insight in the physiological state of lymphoid microenvironments. So far, T-cell behavior, motility and their priming by dendritic cells in peripheral lymph nodes and the thymus have been investigated (Bousso et al., 2002; Miller et al., 2002; Bousso and Robey, 2003; Miller et al., 2003; Mempel et al., 2004a; Mempel et al., 2004b; Miller et al., 2004a; Miller et al., 2004b; Celli et

al., 2005; Mempel et al., 2006; Beltman et al., 2007; Celli et al., 2007; Fischer et al., 2007; Worbs et al., 2007; Henrickson et al., 2008a; Henrickson et al., 2008b). It has been recently shown, that cell migration within the lymph node highly depends on the stromal microanatomy (Bajenoff et al., 2006). Also, the role of natural killer cells within the lymph node has been investigated (Garrod et al., 2007; Celli et al., 2008). The migration of germinal-center B-cells has been revealed to follow a predominant intrazonal circulation pattern (Hauser et al., 2007). Also, there is evidence, that B-cells play a role as antigen transporters into the follicle of the lymph node (Carrasco and Batista, 2007). Lately, this study has in part contributed to immunological research with the application of this technique to the BM organ. Our group found that the BM functions as a major reservoir for T_{CM} (Mazo et al., 2005) and that these cells can even be activated by circulating dendritic cells and consequently trigger recall responses in the BM (Cavanagh et al., 2005). Recently, our group also took advantage of MPM to study thrombopoiesis within BM. They observed megakaryocytes as sessile cells that extended protrusions into microvessels. These proplatelet-like intravascular extensions seemed to be sheared from their stems by blood flow and appeared as proplatelets in peripheral blood, suggesting, that hydrodynamic shear stress could be a determinant of thrombopoiesis (Junt et al., 2007). Nevertheless, the application of MPM to the BM microenvironment is relatively new and will continue to reveal insights in immunology that are so far unknown.

2 Aims of the Study

The present study is aimed at conducting a spatial analysis of the BM microenvironment in the skull of live mice. The advantages of both IVM and MPM were combined to allow the multidimensional investigation of the BM organ in its physiological state for the first time.

However, using a sophisticated imaging technique, such as MPM, one is confronted with several challenges: data acquisition under variable conditions and image processing impair the outcome view on the BM microenvironment, e.g. by different signal intensity and background noise. Possibly the true state of affairs is no longer shown, especially looking at spatial relationships of an organ. Nevertheless, the complexity of the technique involves the need for image processing and analysis techniques to extract meaningful information. How could a standardized image acquisition and processing technique be guaranteed? What would be an adequate representation of spatial relationships in the BM? In theory, MPM offers investigation in the µm-range and below. Former studies already investigated at a cell level in other organs. Does this model allow exploring scenes in the BM microenvironment on a cell-basis?

Therefore, this thesis concentrated on three parts: The first goal was to develop a procedure of image acquisition, processing and analysis to obtain a representative view on the spatial situation in the BM. Raw data sets should be processed and analyzed in a relatively simple, standardized and reproducible way. This part was the main focus of the thesis.

Second, the study aimed at an adequate presentation of spatial relationships in

the BM, especially the context between intravascular space and marrow. Measurements should be performed for both compartments, compromising a maximum of quantitative information and dealing with genuine description of spatial relationships.

After the application of MPM to an *in vivo* mouse BM model and the spatial characterization of this microenvironment it should be emphasized on the subsequent basis for further *in vivo* cell behavior, -migration, -development and cell-cell interaction studies to answer open immunological questions. Therefore, the third part of the thesis included adoptive transfer experiments of certain subsets of lymphocytes: T_{CM} and naïve B-cells. We addressed the question whether one could find these cell populations in different locations in the BM cavity and if there would be any evidence for subcompartmentalization in mouse skull BM.

3 Materials and Methods

3.1 Experimental Design

3.1.1 Place of the Study

The experimental part of this study was performed in the laboratory of Ulrich von Andrian at the IDI Immune Disease Institute, affiliated to Harvard Medical School, in Boston, Massachusetts, USA.

3.1.2 Components

3.1.2.1 Animals

For these studies male and female adult C57/BL6 mice were purchased from Taconics (Germantown, NY). They were used between 10-14 weeks of age with a bodyweight of 20-25 g because BM cavities are well developed at that age and the amount of inactive, fatty marrow relative to active, red marrow is minimal. Animals were kept under viral antigen-free and specific antigen-free conditions on standard laboratory chow and sterile water ad libitum. All experimental procedures were in compliance with National Institutes of Health (NIH) guidelines for the care and use of laboratory animals. Procedures were also approved by the Standing Committees on Animals of Harvard Medical School and the CBR Institute for Biomedical Research.

3.1.2.2 Fluorophores, Antibodies and Reagents

In this study the two compartments of the BM cavity were visualized by fluorescence imaging: the intravascular compartment consisting of arterioles, venules, sinusoids and capillaries and the extravascular compartment consisting mostly of hematopoietic tissue. Two fluorophores were used to delineate these two compartments of the BM: Fluorescein isothiocynate (FITC)-dextran (168 kD MW) and Rhodamine 6G (479 D MW) were purchased from Sigma (St. Louis, MO). FITC-dextran is a water soluble macromolecule often employed for perfusion studies and was used in a dose of 10 µl/g bodyweight (dilution of 2 mg/ml) to label the intravascular space. To stain the extravascular BM compartment consisting of hematopoietic tissue, Rhodamine 6G, a mitochondria dye, was used in a dose of 15 µl/g bodyweight (dilution of 1 mg/ml). Both fluorophores were injected through a jugular vein catheter at the beginning of the experiment, redistributed within intra- and extravascular space of the BM compartment respectively and could be visualized by MPM after a couple of minutes. In all experiments, 50 µl FITC-dextran was administered a second time, approximately 45 minutes after the initial injection, to compensate for the loss of fluorescence presumably due to elimination of the compound and FITC-dextran extravasation.

In adoptive transfer experiments a third fluorophore was used to view injected cells in the BM cavity after homing, in addition to delineating the intra- and extravascular compartment, Hoechst 33342, a nucleic acid stain, purchased from Molecular Probes (Eugene, OR). Cells were always resuspended in labeling media (labeling media contains D-MEM, 1% FBS (fetal bovine serum) and 20 mM HEPES, all bought from GIBCO® product, Invitrogen corporation, Grand Island, NY). Cells were incubated with Hoechst 33342 in a concentration of 0.5 µl/ml cell

suspension (dilution of 10 mg/ml) for 30 minutes at 37°C and centrifuged over a FBS gradient before use.

T-cells were kept in T-cell media containing RPMI 1640 (Bio Whittaker, Walkersville, MD), 10% FBS, 2mM L-glutamine, 10 mM pyruvate, penicillin/streptomycin, 10 mM HEPES (all bought from GIBCO® products, Invitrogen corporation, Grand Island, NY) and 50 µM BME (Sigma-Aldrich).

Human recombinant IL-15 was purchased from R&D Systems Inc., Minneapolis, MN.

All rat anti-mouse antibodies used during FACS analysis were purchased from BD Pharmingen (San Diego, CA): anti- CD3ε; CyChrome-labeled anti-CD4 and anti-CD8; PE-labeled anti-CD44, anti-CD25 and anti-L-selectin, anti-B220; FITC-labeled anti-CD4.

Rat-anti mouse monoclonal antibodies used in negative selection for purification of naïve B-cells from splenocytes were purchased from BD Pharmingen (San Diego, CA): anti-CD3, anti-CD90, anti-Ter-119, anti-Gr-1 and anti-Mac-1. This antibody-cocktail is commonly used for the negative purification of naïve B-cells, targeting T-cells and -precursors, myoblasts, granulocytes, macrophages, natural killer cells, monocytes and cells of erythroid lineage.

3.1.2.3 Cells for Adoptive Transfer Experiments

In adoptive transfer experiments the study compared the homing of two cell populations: CD8+ central memory like T-cells (T_{CM}) and naïve B-cells.

T_{CM} were differentiated from naïve murine T-cells in culture as previously

described (Manjunath et al., 2001; Weninger et al., 2001). Briefly, spleens were dissected from C57/BL6 mice, minced with scissors and sieved through a nylon mesh (Becton Dickinson, San Jose, CA) and rinsed with phosphate-buffered saline (PBS) supplemented with 1% FBS. Isolated cells were washed once. 3 ml ammonium chloride (ACK) buffer (GIBCO® products, Invitrogen corporation, Grand Island, NY) was added for 5 minutes at room temperature for lyses of red blood cells. For neutralization of ACK buffer the tube was filled up with PBS and cells were spun down, washed again and finally resuspended in 10 ml T-cell media. 10 µl anti-mouse CD3ε (was added (1 µg/ml) and cells were cultured in a small tissue-culture flask at 37°C for two days. Cells were then washed with T-cell media, resuspended in fresh tissue-culture flasks in 20 ml T-cell media and 80 µl of IL-15 solution (5 µg/ml) were added. IL-15 was replaced every second day, and T_{CM} were used for adoptive transfer experiments at day 9-11 of culture. Before starting the experiment, viability of the cells was determined by Trypan blue exclusion and the phenotype was verified by 2-color flow cytometry (FACScan™; Becton Dickinson, Franklin Lakes, NJ) using cell size and expression of L-selectin, CD44 and CD25.

For cell-phenotyping by FACS analysis 100 µl of the T-cell culture were applied to individual wells in a 96-well plate. Cells were spun down and resuspended in 100 µl of Fc-block solution, containing PBS with 1% FBS and Fc-block (CD16/32(Fcγ)). Cells were incubated on ice for 10 min. In the mean time, CyChrome-stained anti-CD8 and anti-CD4 solutions were prepared. These solutions were separately added to 3 wells each. PE-stained anti-CD44, -CD25 and -L-selectin were added as well, 1 antibody in one CD4 and in one CD8 well respectively. The plate was again incubated on ice for 15 min., spun down, washed and cells were

resuspended in 150 µl of PBS containing 1% FBS for flow cytometry. As an example of cell phenotype see figure 5 showing that T_{CM} were CD8+, CD4-, CD25 low, CD44 high and L-selectin intermediate.

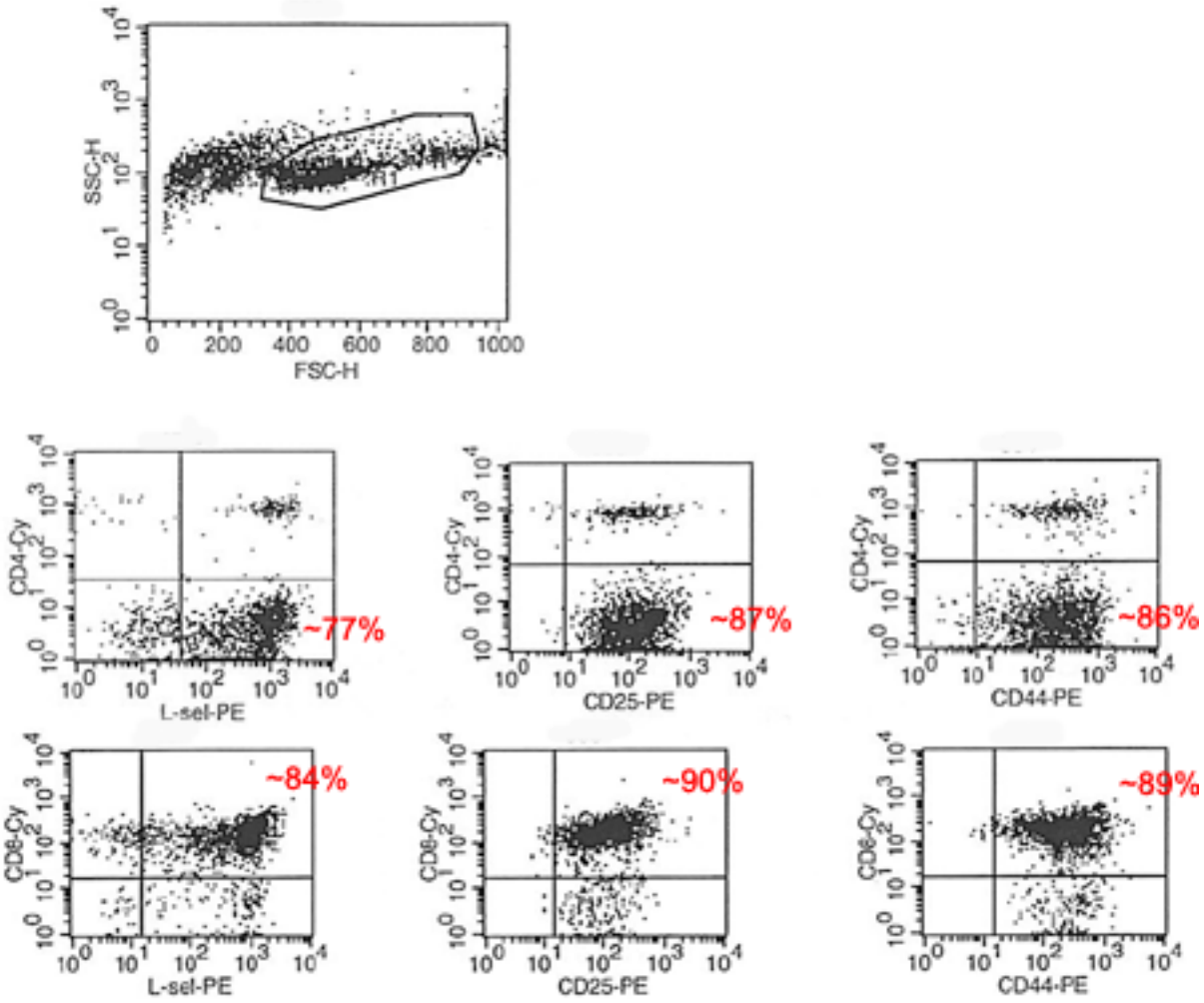

Figure 5. Phenotype of T_{CM}

FACS analysis of a cell culture at day 8: Cells were checked for CD4 (top row, y-axis) and CD8 (bottom row, y-axis) compared to the expression of L-selectin, CD25 and CD44 (x-axis). After gating on life cells ~90% of CD8+ cells were also L-selectin high and expressed CD25 and CD44. CD25 expression is described as intermediate. ~ 85% were CD4 negative when L-selectin, CD25 and CD44 were expressed.

Since the spleen harbors a large number of naïve B-cells (Figure 6), spleens from adult C57/BL6 mice were found to be an adequate source to obtain naïve B-cells for adoptive transfer experiments. Spleen tissue was first minced with scissors and then squeezed through a nylon mesh. Cells were washed and red blood cells were lysed with ACK. The fraction of B220-positive cells among total splenocytes was ~60% as determined by FACS analysis (Figure 6) (description of FACS analysis see below).

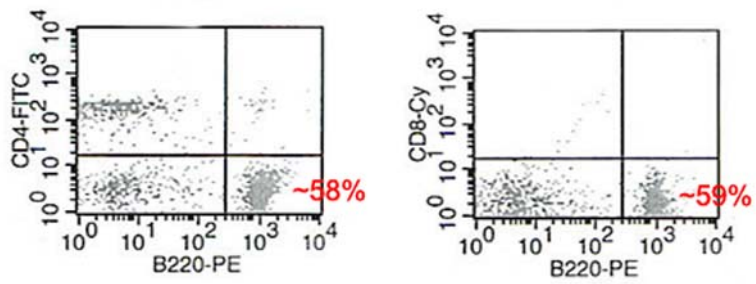

Figure 6. Phenotype of total splenocytes

FACS analysis after isolation from spleens of C57/BL6 mice when gated on life cells: ~60% of splenocytes expressed the B-cell marker B220 (x-axis) and were CD4 (left panel, y-axis) and CD8 (right panel, y-axis) negative before purification of B-cell fraction from total splenocytes.

Naïve B-cells were purified from splenocytes by negative selection using a immunomagnetic MACS purification protocol (Miltenyi Biotec, Auburn, CA), meaning that all splenocytes except naïve B-cells were labeled with antibody-conjugated magnetic particles and were therefore retained in a magnetic separation column. Briefly, washed splenocytes were resuspended in 500 µl of PBS containing 1% FBS. Cells were then incubated with the following antibodies: 10 µl of anti-CD3 and 5 µl of each anti-CD90, -Ter119, -Mac-1 and -GR-1 were

added and incubated for 10-15 min. at room temperature. The tube was then filled up to 45 ml with PBS containing 1% FBS, spun down and again incubated in 800 µl buffer and goat-anti-rat-IgG magnetic microbeads according to cell number and the MACS protocol for 15 min. at 4°C. A LD column was placed into the magnetic field of a MACS separator, washed and the cell-magnetic-bead-solution was applied on top of the depletion column. Antibody-conjugated-magnetically labeled cells were retained and after CD3-, CD90-, Ter-119-, GR-1- and Mac-1-negative cells (B-cells) passed through the column, the column was rinsed again and the total effluent was collected containing the enlarged fraction of naïve B-cells. The purification process was performed along the protocol for MACS/LD column by Miltenyi Biotec (for illustration see Figure 7) and is commonly used.

Splenocytes except naïve B-cells (yellow, green, orange) were magnetically labeled with MACS MicroBeads conjugated to anti-CD3, -CD90, -Ter119, -Mac-1 and -GR-1. B-cells (purple) are not labeled.

Labeled cells were retained in a MACS Column.

B-cells (purple) passed through the column and were collected as the enriched, unlabeled fraction depleted of other splenocytes.

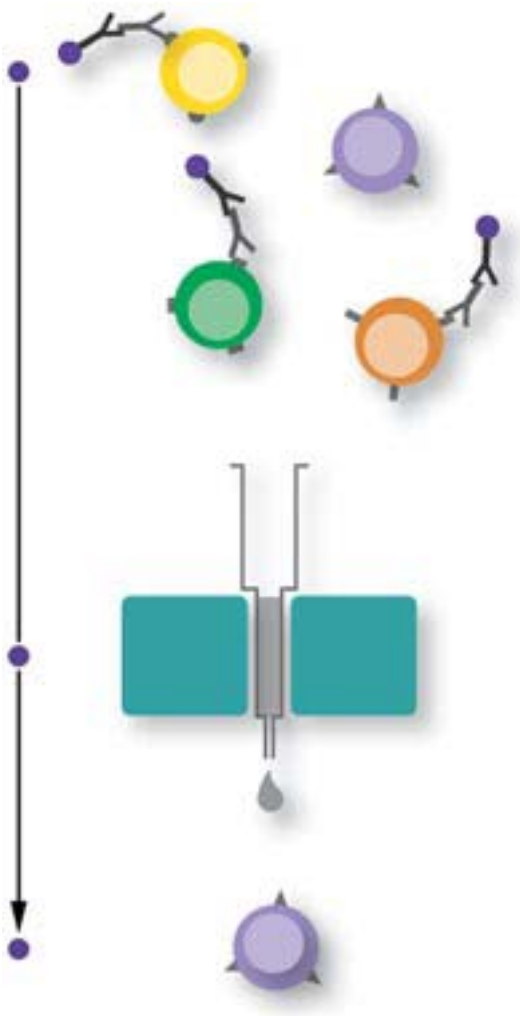

Figure 7. MACS purification of naïve B-cells by negative selection

Figure by Miltenyi Biotec-MACS (Miltenyi Biotec, Auburn, CA).

Using the negative selection technique an enrichment to ~90% of naïve B-cells could be achieved (Figure 8).

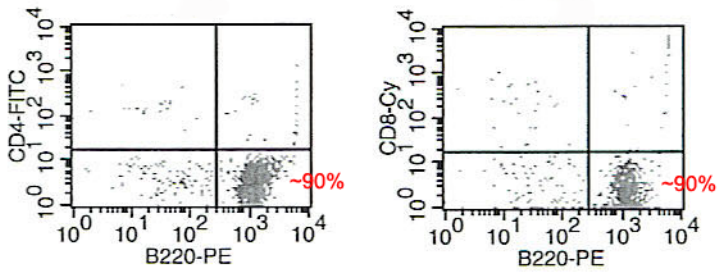

Figure 8. Phenotype of enriched naïve B-cells

After purification of the B-cell fraction of total splenocytes by MACS purification system ~90% viable cells expressed the B-cell marker B220 (x-axis) and were CD4 (left panel, y-axis) and CD8 (right panel, y-axis) negative.

Phenotype and fraction of cells before and after the purification were checked by FACS analysis. 200 µl of the cell samples were applied to individual wells in a 96-well plate. To each well PE-stained anti-B220 was added plus either CyChrome-stained anti-CD8 or FITC-stained anti-CD4. The plate was incubated on ice for 15 min., washed and resuspended in 150 µl PBS containing 1% FBS for analysis. Figure 6 and 8 exemplify FACS analysis before and after negative selection of naïve B-cells (B220+, CD4- and CD8-) by MACS.

For adoptive transfer experiments cells were then fluorescently labeled with Hoechst 33342. Depending on the experiment either cultured T_{CM} or purified naïve B-cells were counted and then resuspended in labeling media (5 mio./ml). Cells were labeled with Hoechst 33342 (see 3.1.2.2). In each experiment 30-50 million cells were injected into the tail vein of the recipient mouse. 2 or 24 hours after the injection multiphoton experiments were performed to locate the cells in the BM microenvironment.

3.1.3 Preparation of the Animal

The surgical preparation of the mouse was performed as previously described (Mazo et al., 1998). Briefly, mice were anesthetized by intraperitoneal injection (10 µl/g) of physiologic saline containing ketamine (dilution of 5 mg/ml) and xylazine (dilution of 1 mg/ml). The body temperature was monitored during the preparation and throughout the experiment. Hair removal lotion (Nair, Carter Products, NY) was used to remove the hair on the scalp to expose the skull and in the right submandibular region of the neck to place the catheter. A skin incision was made in this region of the neck and the jugular vein and the common carotid artery was exposed. A PE-10 catheter (Becton Dickinson, Franklin Lakes, NJ) was inserted in the right jugular vein for injection of fluorophores and in the right common carotid artery for application of fluorescently labeled cells in adoptive transfer experiments. In the midline of the scalp another incision was made and a plastic ring was inserted to access the frontoparietal region of the skull BM while avoiding damage to the bone tissue. To prevent drying of the tissue physiologic, saline was applied into the ring. After the surgical preparation, the mouse was placed on a stage equipped with a stereotactic holder. The immobilized head was gently tilted using fine adjustment screws of the stereotactic holder. This immobilization technique was crucial in minimizing movement artifacts (Figure 9).

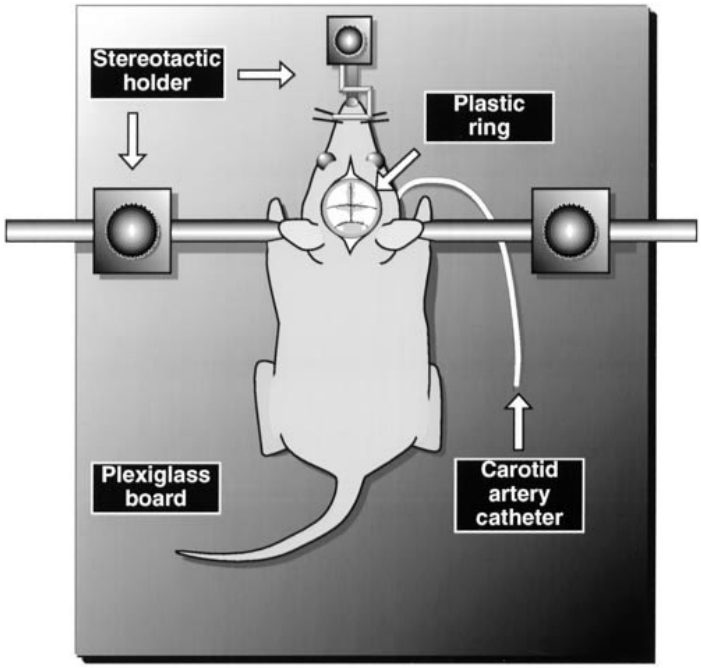

Figure 9. Animal preparation and immobilization technique of the mouse

The BM region is exposed by inserting a plastic ring in the skin of the mouse calvaria. The skull itself is placed and fixed with a stereotactic holder to prevent movement during the experiment. Figure from Mazo *et al.(Mazo and Von Andrian, 1999)*

To position the exposed frontoparietal region of the BM in a horizontal plane suitable for microscopic viewing, the immobilized mouse was fixed on another stage which allowed fine adjustments in this plane. Subsequently, the animal was placed on the imaging stage of the multiphoton microscope. To prevent of hypothermia this microscope stage was covered with a plastic sheet. The temperature under this sheet was controlled by infrared lamp illumination.

3.1.4 Intravital Microscopy Experiments

3.1.4.1 Multiphoton Microscopy Setup

The MPM system used in this study was a custom modified Olympus BX 50 WI upright microscope coupled to a mode-locked Tsunami Ti:sapphire laser (Spectra Physics, Mountain View, CA) and a Radiance 2000 MP confocal multiphoton imaging system controlled by Lasersharp software (Biorad Laboratories, Hemel Hempstead, UK). For the configuration of the microscope's components see Figure 10.

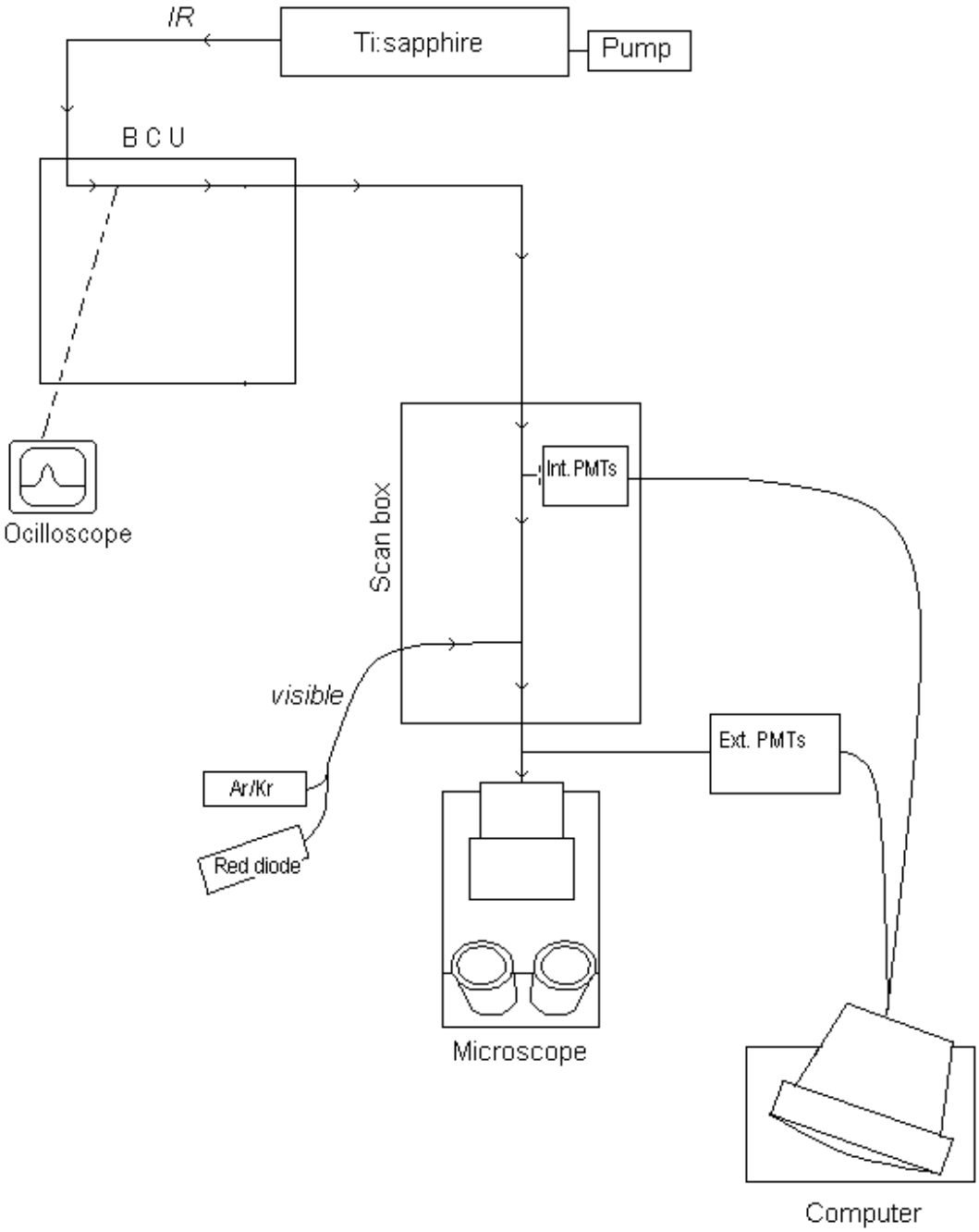

Figure 10. Configuration of the MPM system

A Ti:sapphire laser (spectral range of 690-1000 nm, pulse widths of 100 fs) is used at an excitation wavelength of 800 nm. The properties of the infra-red (IR) beam are optimized by the beam conditioning unit (BCU). It is directed via a Scanbox to the microscope. Resulting emission is detected by external detectors (ext. PMTs) depending on used fluorophores and processed by adequate computer software. Ar/Kr, Red diode lasers and internal detectors (int. PMTs) are components of a confocal microscope that in our laboratory was coupled to the microscopy system.

The laser was tuned to a wavelength of 800 nm to simultaneously excite all fluorophores that were used. Two different raw data sets of images were collected: Overviews of the frontoparietal BM compartment were taken with a 10 x WI lens (NA 0.3) (Olympus, Japan). A 40 x WI lens (NA 0.8) (Olympus, Japan) was used for high resolution data acquisition to perform 3D quantitative analysis and for adoptive transfer experiments. The intravascular space labeled with FITC-dextran was detected through bandpass emission detectors at 525 / 30 nm and the extravascular space labeled with Rhodamine 6G was detected at 620 / 100 nm. A third detector of 400 / 40 nm was used to capture the combined autofluorescence and second harmonic emissions of the surrounding connective tissue matrix and the bone tissue. In adoptive transfer experiments, injected cells labeled with Hoechst 33342 were detected at 450 / 80 nm.

In order to minimize systemic errors in quantitative results, it was necessary to check certain parameters of the microscope system throughout the course of this study. A laser power of 40% was used during the entire study. Other settings of the microscope system, such as “gain” and “offset”, were adjusted in a standardized way in each experiment to minimize differences in intensity values. Also, the imaging system was calibrated with a magnification reference standard (MRS-3, Geller Microanalytical Laboratory, Topsfield, MA) and the accuracy of the computer-controlled Z-step motor was routinely checked using a commonly available calibration device (Geller Microanalytical Laboratory, Topsfield, MA).

3.1.4.2 Quantification of Bone Marrow

All required preparations and basic settings of the microscope system were described in the previous paragraphs. In the following, we will describe the course of a typical experiment.

After the surgical preparation and positioning of the animal for microscopic viewing (described in 3.1.3) the fluorophores FITC-dextran and Rhodamine 6G were intravenously applied (see 3.1.2.2).

First, data sets for quantitative analysis of single BM regions were collected. Z-series image stacks of different microvascular segments were taken with a 40 x WI objective (NA 0.8). Volumes with a size of 307 x 307 µm and a depth of 90-150 µm (1 µm Z-step size) were obtained. Figure 11 illustrates the performance of such an experiment. Image acquisition in general results in 1 image stack. However, this stack is displayed in 3 individual channels: red, green and blue. Merging these 3 channels results in the common display of a 3-color-image.

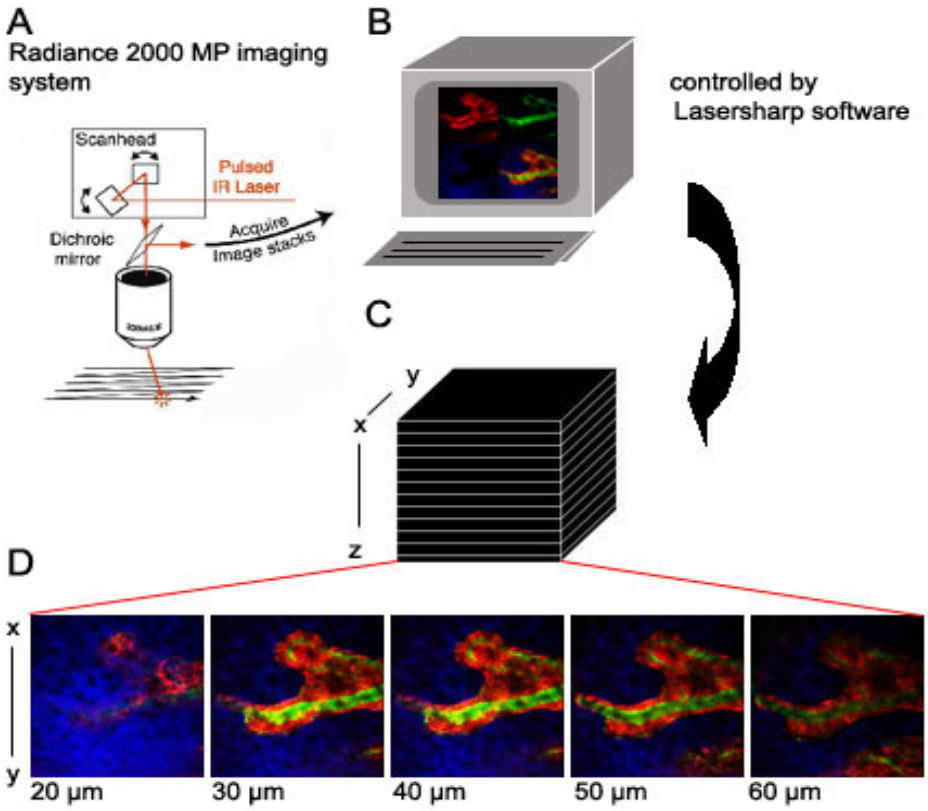

Figure 11. Image acquisition during the experiment

(A) Image acquisition by a Radiance 2000 MP (multiphoton) imaging system: a pulsed beam of infrared (IR) laser light is raster scanned via the microscope objective onto the specimen by rapid, synchronized movement of a pair of steering mirrors (Figure and legend by (Sumen et al., 2004)). (B) Image collection is controlled by Lasersharp software. 3 channels and a merged image of 3 channels are displayed (C) Volumes are generated by the collection of stacks of XY-images (optical sections) (D) As an example of Z-stack collection see single sections (307 x 307 µm) of an intermediate BM venule at various depth.

For subsequent measurements and analysis we selected areas where single vessels and the surrounding BM were clearly detectable. Additional XZ-scans (vertical sections / side views) of these areas were also collected as reference images to 3D reconstructed image stacks. During one experiment it was possible to generate about 5-8 raw data sets of different microvascular segments. At the

end of each experiment overviews of the vascular structure in the frontoparietal region of the skull BM were collected using a 10 x WI (NA 0.3) objective. Volumes with a size of 1234 x 1234 µm and a depth of 100-300 µm depth (Z-step size 10 µm) were scanned. XY-projections of these image stacks were put together to a “montage” providing an overview of the total frontoparietal BM compartment imaged in one experiment (Figure 12).

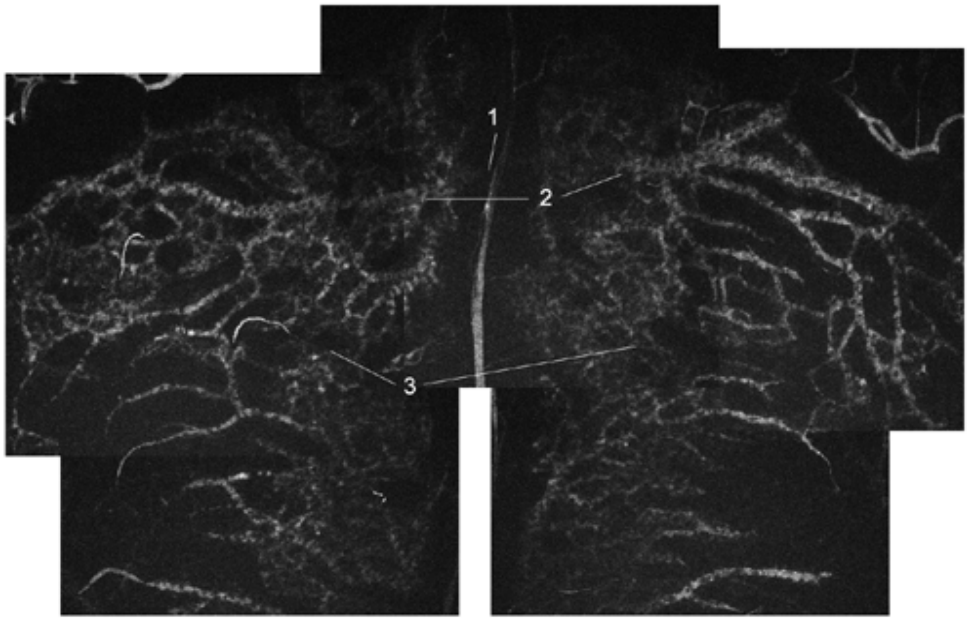

Figure 12. “Montage” of the BM region investigated during one experiment

XY-Projections of 5 volumes were put together to a montage of the total investigated area of the BM vasculature of one experiment. For orientation the superior sagittal sinus is shown in the midline (1). The left and right CV (2) and broad network of S are displayed. (Image size represents ~3.1 x 2.1 mm).

3.1.4.3 Adoptive Transfer Experiments

In adoptive transfer experiments purified naïve B-cells or T_{CM} (see 3.1.2.3) were injected into a tail vein of a recipient mouse before starting the experiment. 2 or 24 hours after cell injection, IVM experiments were performed. Data acquisition was the same as to the procedure explained in 3.1.4.2. Additionally to Z-series image stacks, XZ-scans (vertical sections / side views) were collected along a scanline of an XY-image in the area of a migrated cell. This technique allowed measurements of two distances: 1. the shortest distance between the centroid of an emigrated cell and the vessel wall; 2.the distance from the vessel wall to the end of the BM cavity in this line (for measurements see 3.2.2). Therefore, the scanline to obtain a side view was placed perpendicular to the vessel axis and through the midpoint of a single extravasated cell. This step of data acquisition is demonstrated in Figure 13. In these experiments a 40 x WI (NA 0.8) lens was used with a digital zoom factor of 2.0.

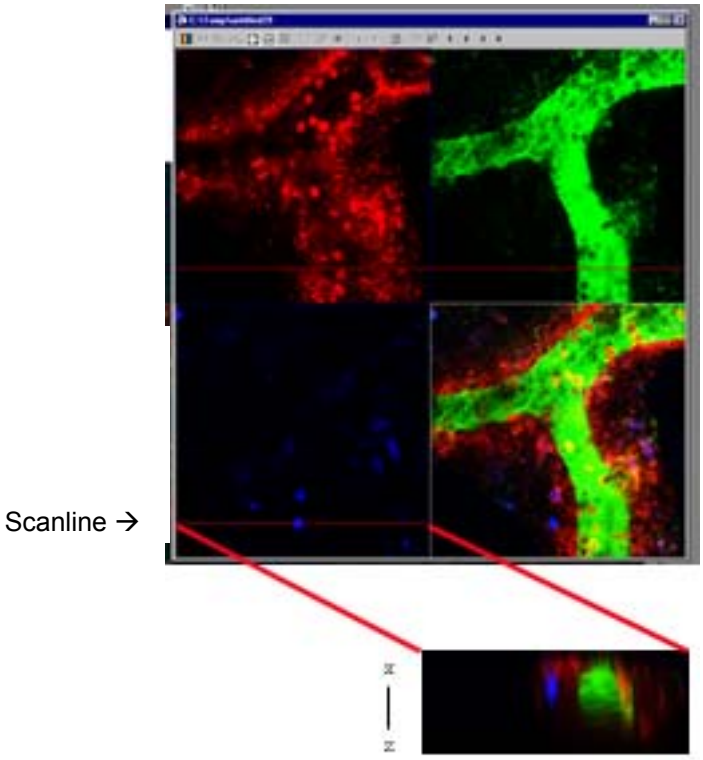

Figure 13. Additional Image Acquisition in Adoptive Transfer Experiments

In the top part of the figure the 3 channels of one XY-image are shown (red, green, blue) and the additional merged XY-image. On the basis of a migrated cell (blue channel) a scanline was chosen. Based on this scanline a XZ-side view (vertical section) was collected (bottom of the figure). In this area a single extravasated cell lay perpendicular to the vessel. Based on these XZ-scans distance measurements were performed.

3.2 Image Processing and Analysis

3.2.1 Quantification of Bone Marrow

Collected raw data sets (see 3.1.4.2) were processed for further analysis as follows: We aimed to present the spatial relationships of the BM compartment as the ratio of intravascular to extravascular space. Therefore, quantitative measurements were performed for two compartments: first, the intravascular

volume of a microvascular segment and second, the volume of the total BM compartment that contained this particular microvascular segment. Measurements of intravascular BM space were carried out on Z-stacks of FITC-dextran-channel displaying filled microvessels. The total BM compartment (intra- and extravascular space) was captured using merged FITC-dextran / Rhodamine 6G stained Z-series image stacks. We will refer to these two compartments as area of interest (AOI) in the paragraph below.

The measurement software VoxBlast (V. 3.1, Vay Tek Inc., IA) was used to for quantitative analysis of AOI. VoxBlast offers an “automatic tracing”-function, which operates on the basis of either excluding or including certain grayscale values into measurements. Provided that the entire image displays only two parts, AOI and background noise, the background noise acquired during image collection had to be excluded, because such noise would interfere with the measurement of AOI. Therefore, the area of background noise had to be given the grayscale value of 0 (on a scale of 0-255). VoxBlast was then instructed to count only the AOI having a grayscale value >0, i.e. 1-255. The graphics software Photoshop (V. 6.0, Adobe Systems Inc., San Jose, CA) proved to be very capable for image processing to change the grayscale value of the background noise to 0. Multiple steps of image processing were programmed as macros (named “actions” in Adobe Photoshop). Single steps were recorded with the “action”-tool and then applied to a whole stack of raw image data for automated processing. Since Photoshop does not readily support the microscope’s proprietary data files, raw data sets were converted to the TIFF file format before processing.

Single processing steps in Adobe Photoshop are outlined in figure 14: First, the “crop”-tool was used to cut out a single venule with its surrounding BM (Figure

14a). The second part of the macro included a thresholding technique to define the background area. Briefly, background noise (in this study mostly having a grayscale value of 0-30) was selected using the “magic wand” (Figure 14b). It is possible, to assign this tool a certain intensity value. For example, when the “magic wand”-tool was set to an intensity value of 25, clicking on a grayscale level of 0 in the background area, the complete background area having a grayscale level of 0-25 was selected. An intensity value of 20-25 for the “magic wand” was used throughout the study. To effectively exclude all background noise without affecting the actual AOI (intravascular volume in FITC-dextran-stacks and total BM cavity volume in merged FITC-dextran / Rhodamine 6G stained stacks), the selected area was first “expanded” (Figure 14c); in FITC-dextran stained stacks by 1 px, in merged FITC-dextran / Rhodamine 6G stained stacks by 2 px and then “contracted” (Figure 14d); in merged FITC-dextran / Rhodamine 6G stained stacks by 2 px. Subsequent “smoothing” the AOI by 10 px resulted in a better visual presentation (Figure 14e) and did not affect quantitative measurements (Comparisons of resulting measurements of AOI using the “smooth”-step and without this step in 5 examples did not show significant differences). Terminating, the selected background was filled black (grayscale level of 0) (Figure 14f).

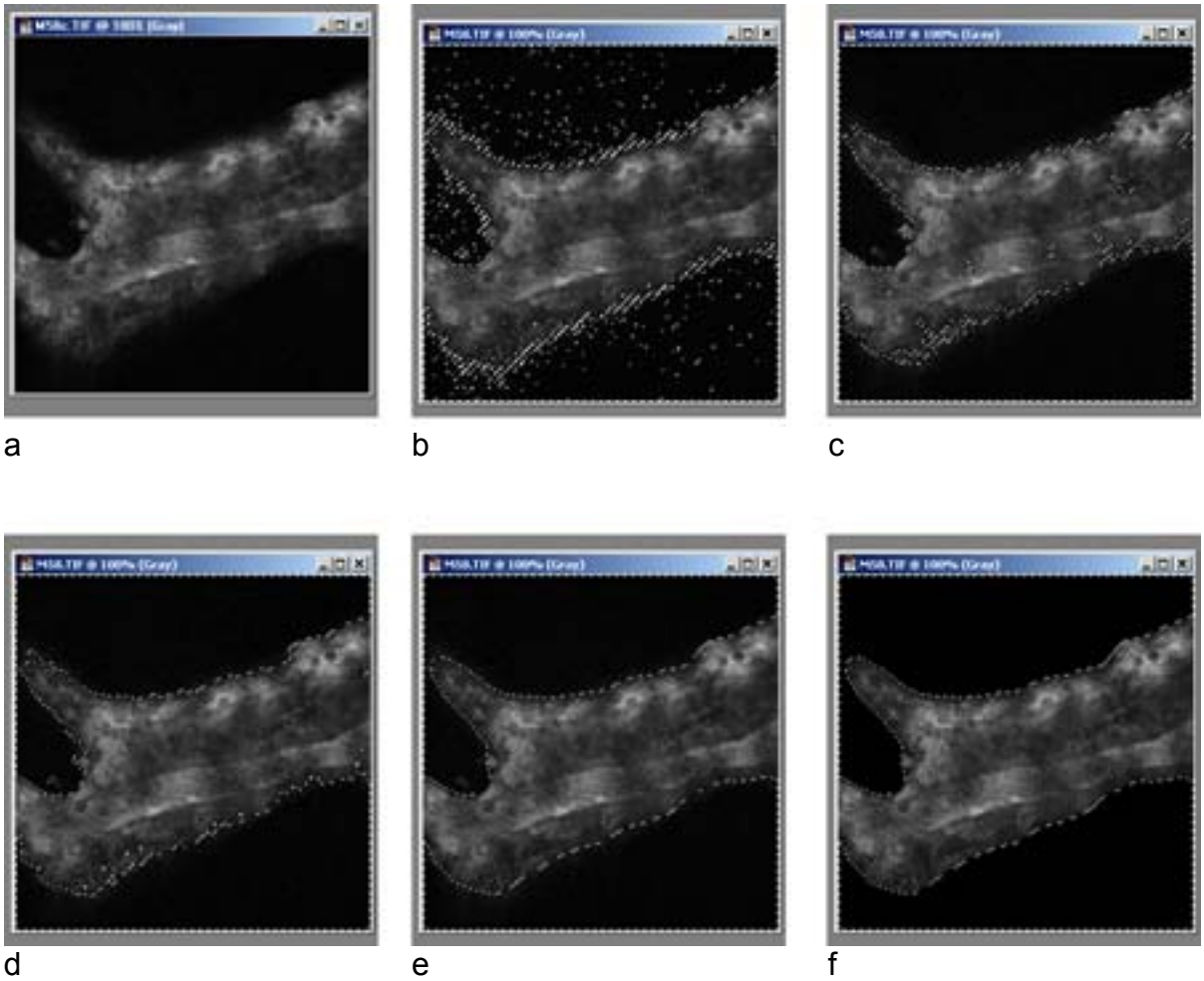

Figure 14. Image processing technique in Adobe Photoshop

Demonstrated on one section of a merged FITC-dextran / Rhodamine 6G image stack: (a) a single vessel with surrounding marrow (AOI) was “cropped” out of the image. (b) The background was selected using the “magic wand” with an intensity value of 20-25. (c) “expanding” and (d) “contracting” the selected background effectively excluded all background noise. (e) the “smooth”-tool was used for better visual representation and (f) the complete background was filled black.

Figure 15 shows a comparison of one section of a raw data image stack and the corresponding final processed section.

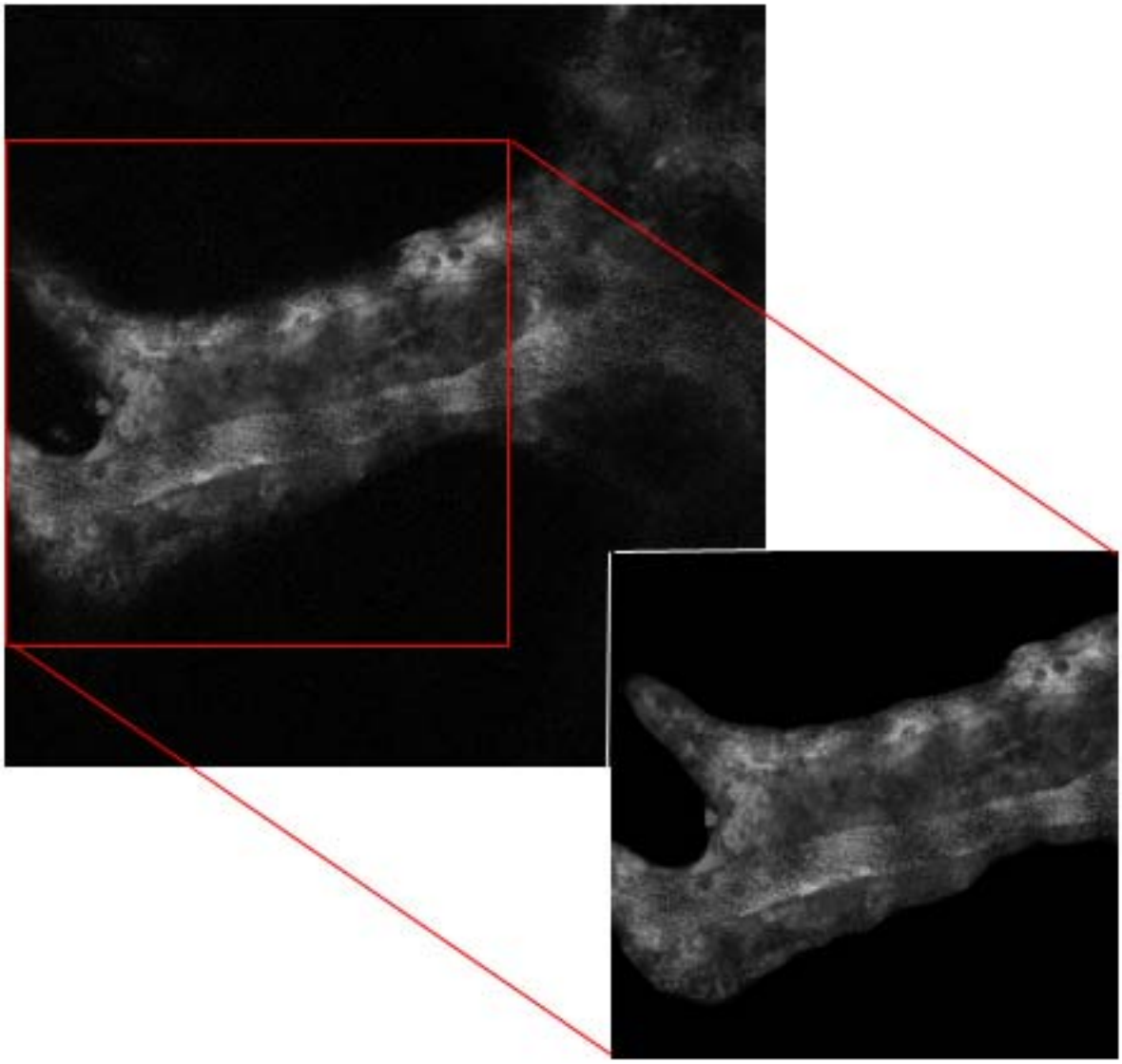

Figure 15. Comparison of a raw data section with its corresponding processed section

These image processing steps were separately recorded in Adobe Photoshop as an “action” for one section only displaying the FITC-dextran channel and for the corresponding section displaying the merged FITC-dextran and Rhodamine 6G channels. The action was then automatically performed on all sections of the 2 complete image stacks.

Processed image stacks were then imported into the measurement software

VoxBlast for quantitative analysis. As previously explained above, we exploited VoxBlast's "automatic tracing"-function of an AOI on the basis of grayscale values. Image processing in this study generated data that showed background as the minimal grayscale value (grayscale value 0), so that "automatic tracing" could be applied to processed data sets by excluding the background from measurements (Figure 16).

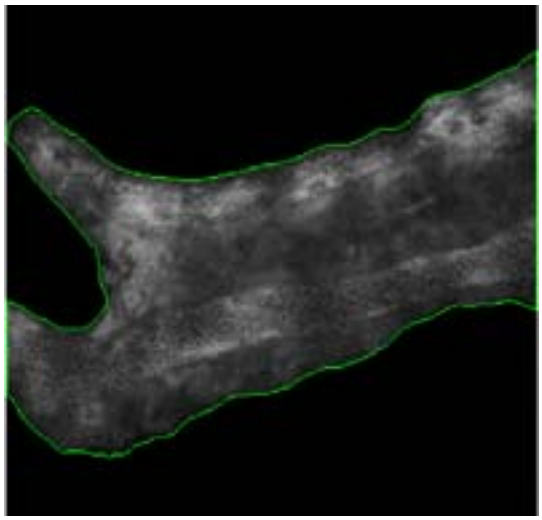

Figure 16. Measurement performance by VoxBlast

Exemplified on one processed, merged FITC-dextran / Rhodamine 6G section, VoxBlast automatically measured the area framed in green, with the setting to count grayscale values of 1-255, the background area with the grayscale value 0 is excluded from the measurements. In this manner, a total processed image stack is measured, pixel values of each section are summated in the end to the pixel volume of one stack and are displayed in VoxBlast.

A quantitative view on a 3D volume was derived from the sum of all measured areas of single sections of a total image stack. Since volumes were derived for the intravascular space and for the total BM cavity (intra- plus extravascular space),

the volume of the extravascular space was derived by subtracting the intravascular volume from the volume of the total BM compartment. Subsequently, the ratio of intra- to extravascular space was calculated for different microvascular segments. This image processing technique described above was newly created for this study; a manuscript describing this method is currently in preparation.

3.2.2 Adoptive Transfer Experiments

Adoptive transfer experiments were performed for naïve B-cells and T_{CM}. We aimed at comparing the localization of these different cells in the BM at two time points. Therefore, we measured the closest distance between an extravasated cell and the vessels wall. XZ-scans (vertical sections / side views) that show a cross-section of a fluorescent extravascular cell perpendicular to a vessel were taken along a scanline that was individually chosen according to the vessel axis (Figure 17, for measurement methodology see Figure 13 and explanation in 3.1.4.3) and were analyzed using Adobe Photoshop software. The “ruler”-tool in Adobe Photoshop was used to measure the shortest distance from the vessel wall to the midpoint of the emigrated cell (Figure 17, top) and to the outer margin of the BM cavity (Figure17, bottom). Distances were measured three times and are shown as the mean.

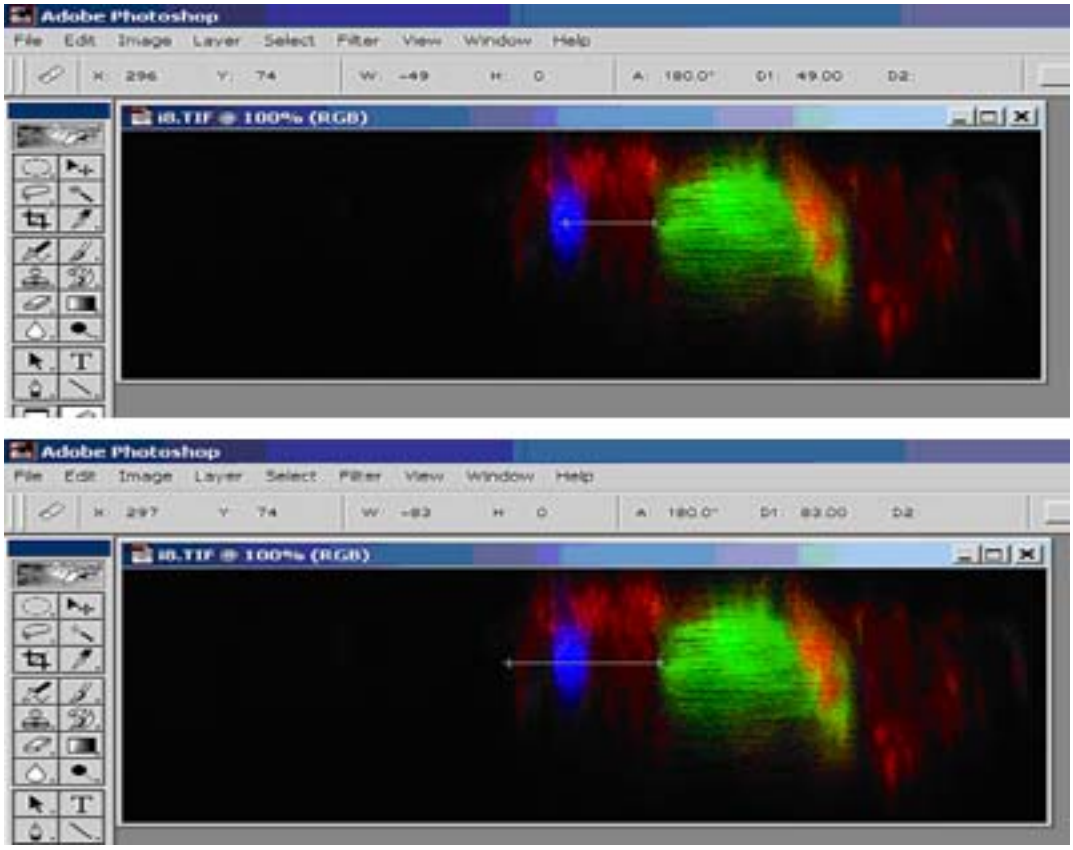

Figure 17. Image analysis in adoptive transfer experiments

Adobe Photoshop was used to perform distance measurements in adoptive transfer experiments. The ”ruler” measured the shortest distance of the vessel wall to the midpoint of the migrated cell (top panel) and to the outer margin of the BM cavity (bottom panel).

3.2.3 Vessel Diameter Measurements

Diameters of different microvascular segments were derived from measurements on reconstructed XY-projections of FITC-stained stacks. The cross-sectional diameter of each vessel was measured 3 times with the “ruler”-tool of Adobe Photoshop and results are shown as mean values.

3.2.4 3D Reconstruction from Processed Image Stacks

For 3D reconstruction view of a single microvascular segment of the BM organ movies were generated using VoxBlast. Movies were generated showing a 360° rotation of a single reconstructed microvascular segment along a virtual axis. Before imparting processed image stacks for reconstruction, the image stack viewing the microvessel was subtracted from the merged FITC-dextran / Rhodamine 6G stack using Adobe Photoshop. Resulting data sets were reloaded in VoxBlast and brightness and transparency were individually chosen in the "Palette Editor" to create 3D reconstructed movies. In adoptive transfer experiments a third data set was loaded before starting the movie generation to additionally visualize homed cells in the BM compartment.

3.3 Statistics

3.3.1 Bone Marrow Quantification

For BM quantification results were expressed as ratios of intra- to extravascular space for different microvascular segments. Mean values of ratios for different microvascular segments were compared in the total group using Anova and the Kruskal-Wallis test. Differences were considered statistically significant when $p < 0.05$.

3.3.2 Adoptive Transfer Experiments

In adoptive transfer experiments regression analysis were performed, describing how far a single cell migrated away from the closest vessel relative to the maximal

distance possible. We compared the slopes of regression lines with the 95%-confidence intervals for naïve B-cells and T_{CM} after 2 and 24 hour homing, respectively, and the two cell types among each other.

4 Results

4.1 Anatomy and Morphology of the Bone Marrow

The BM microenvironment lies within cavities of long and flat bones and consists of hematopoietic tissue that is penetrated by numerous microvessels. In this experimental setup a physiologically perfused BM microenvironment was investigated in the mouse skull. Figure 18 shows an overview of the imaged part of the BM and the anatomical position of different microvascular segments. The superior sagittal sinus (6) runs through the centerline of the skull frontal to occipital direction. CV (1) drain almost perpendicularly into the superior sagittal sinus and collect blood from a network of laterally located IV (3). The CV also receives blood from a network of S (4), either directly or via one or more PSV (2). Blood from the dense parasagittal CN (5) drains directly into the sagittal sinus. The anatomy of these venous segments has been characterized first by our group by epifluorescence microscopy and histology (Mazo et al., 1998) (see 1.1.3). This morphology could be confirmed by a multidimensional view using the intravital MPM (for methodology see 3.1.4.2). The microvascular anatomy of the mouse skull BM has been well established and will not be further discussed here.

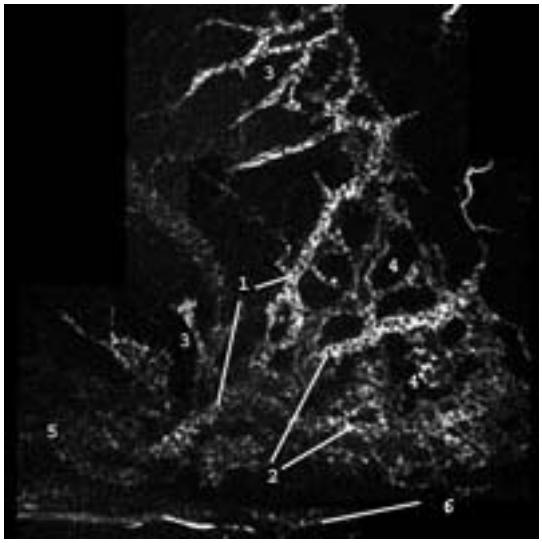

Figure 18. Arrangement of microvascular segments in the frontoparietal region of skull BM

A CV (1) collects blood from IV (3) and runs into the superior sagittal sinus (6), which runs horizontal at the bottom of this figure. Blood from S (4) drains either directly or via a PSV (2) into the CV (1). Venules of the CN (5) release their blood into the superior sagittal sinus (6). Projection of an image stack taken with a 10xWI objective (image size ~1.2 mm x ~1.2 mm).

Exemplifying the 3D view of a single microvascular segment embedded in hematopoietic tissue within the bone, figure 19 illustrates a BM microvessel at various depths below the skull surface (for methodology see 3.1.4.2). An IV surrounded by hematopoietic tissue was visualized by the fluorescence distribution of FITC-dextran and Rhodamine 6G, the bone tissue was viewed by autofluorescence and second harmonic generation. Thickness of covering bone tissue varied between 20-50 µm depending on area within BM region and mouse. Single sections of a raw data stack are shown (Figure 19).

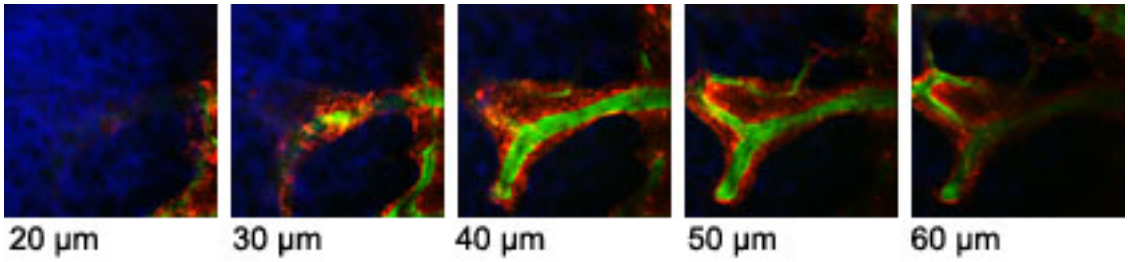

Figure 19. IV at different depth below skull surface

From an image stack obtained by a 40xWI objective (307 µm x 307 µm): Viewed in green (FITC-dextran) the intravascular space, in red (Rhodamine 6G) representing the surrounding hematopoietic tissue and visualized in blue (autofluorescence and second harmonic generation) the bone tissue.

4.2 Quantification of Bone Marrow Compartments

Before quantitative analysis could be performed based on acquired MPM data (see 3.1.4), an image processing technique had to be performed. The design of this technique was a major part of this thesis and is explained in detail in 3.2.1.

Quantification of the BM microenvironment was realized by comparing the intravascular volume and hematopoietic tissue in different anatomical sections. Figure 20 shows the spatial relationship of hematopoietic tissue and BM microvessels as the ratio of intra- to extravascular space on the y-axis plotted for different microvascular segments. This analysis reveals that the microvascular segments can be divided into two groups: IV, S and microvessels of the CN had a ratio of ~0.5, i.e. the extravascular cell volume was twice as large as the intravascular volume, whereas CV and PSV had a ratio of ~1.0, i.e. the volumes of intravascular and extravascular space were approximately equal. These results showed a highly significant correlation by Anova with a p-value < 0.0001. This could be confirmed with the Kruskal-Wallis test.

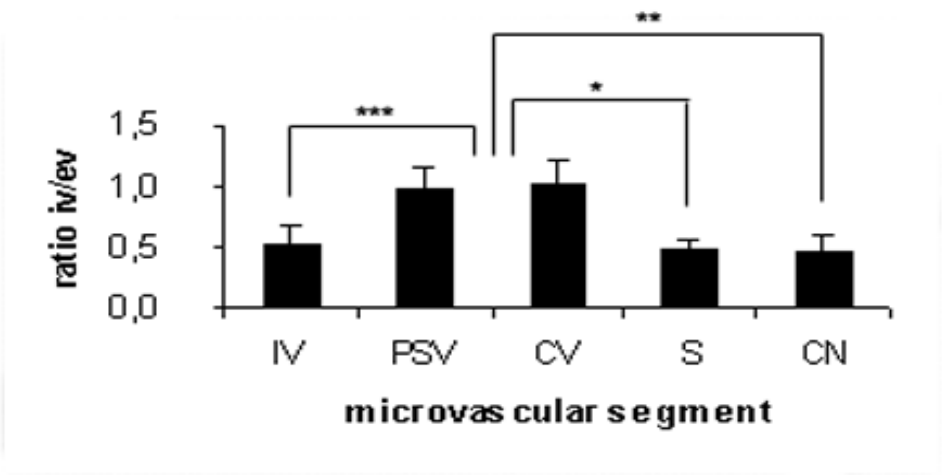

Figure 20. Spatial relationships of BM compartments in different microvascular segments

On the y-axis the ratio of intravascular to extravascular space and on the x-axis the different microvascular segments are plotted. Bars show mean values with standard deviation. IV had a ratio of 0.51 (SD 0.18), S of 0.48 (SD 0.09) and venules of CN had a ratio of 0.46 (SD 0.12). PSV had a ratio of 0.98 (SD 0.18) and CV of 1.02 (SD 0.18). Groups were controlled with each other using the Kruskal-Wallis test (* $p<0.05$, ** $p<0.01$, *** $p<0.001$).

The relative volume of hematopoietic tissue compared to the intravascular volume was in inverse proportion to the vessel diameter. Table 1 shows a summary of vessel diameter and BM quantification with regard to the different microvascular segments. IV, S and microvessels of the CN had a diameter in the range of 21.6-25.6 µm and a ratio of intra- to extravascular volume of ~0.5, whereas BM cavities in regions of CV and PSV with a diameter in the range of 56.6-64.0 µm had a ratio of ~1.0 (Table 1) (for methodology see 3.2.3).

Parameters	**IV**	**PSV**	**CV**	**S**	**CN**
n(venules/animals)	25/6	6/6	18/6	18/6	23/6
Diameter(µm)	**25.59**	**56.56**	**64.04**	**25.09**	**21.56**
SD	7.02	10.15	8.47	7.08	5.01
n(venules/animals)	32/10	6/4	4/4	4/4	10/4
Ratio	**0.51**	**0.98**	**1.03**	**0.48**	**0.46**
SD	0.18	0.18	0.18	0.10	0.12

Table 1. Diameters and ratios of intravascular to extravascular space for different microvascular segments

Measurements of vessel diameters were in line with results obtained by conventional epifluorescence microscopy by Mazo *et al.* (Table 2), except for S, which had a smaller diameter and CV, which had a slightly bigger diameter in the present study (Mazo and Von Andrian, 1999). CN was not investigated by Mazo.

Parameters	BMCV	BM sin.	BMPSV	BMIV
n of venules	16	14	5	19
Diameter (µm)	51.7 ± 22.9 (27.4–99.7)	41.9 ± 10.8 (21.9–60.2)	56.2 ± 11.9 (47.6–74.8)	28.8 ± 9.1 (17.0–50.4)

Table 2. Dimensions of BM microvessels by Mazo *et. al.*

Data are presented as arithmetic mean and SD. Figure by Mazo *et al.* (Mazo and Von Andrian, 1999)

As an example of the spatial relationships in skull BM, Figure 21 shows a microvessel surrounded by hematopoietic tissue in 6 frames of a 3D reconstructed 360° rotation. BM tissue is shown in red (Rhodamine 6G staining) penetrated by an IV visualized in green (FITC-dextran staining) (for methodology see 3.2.4).

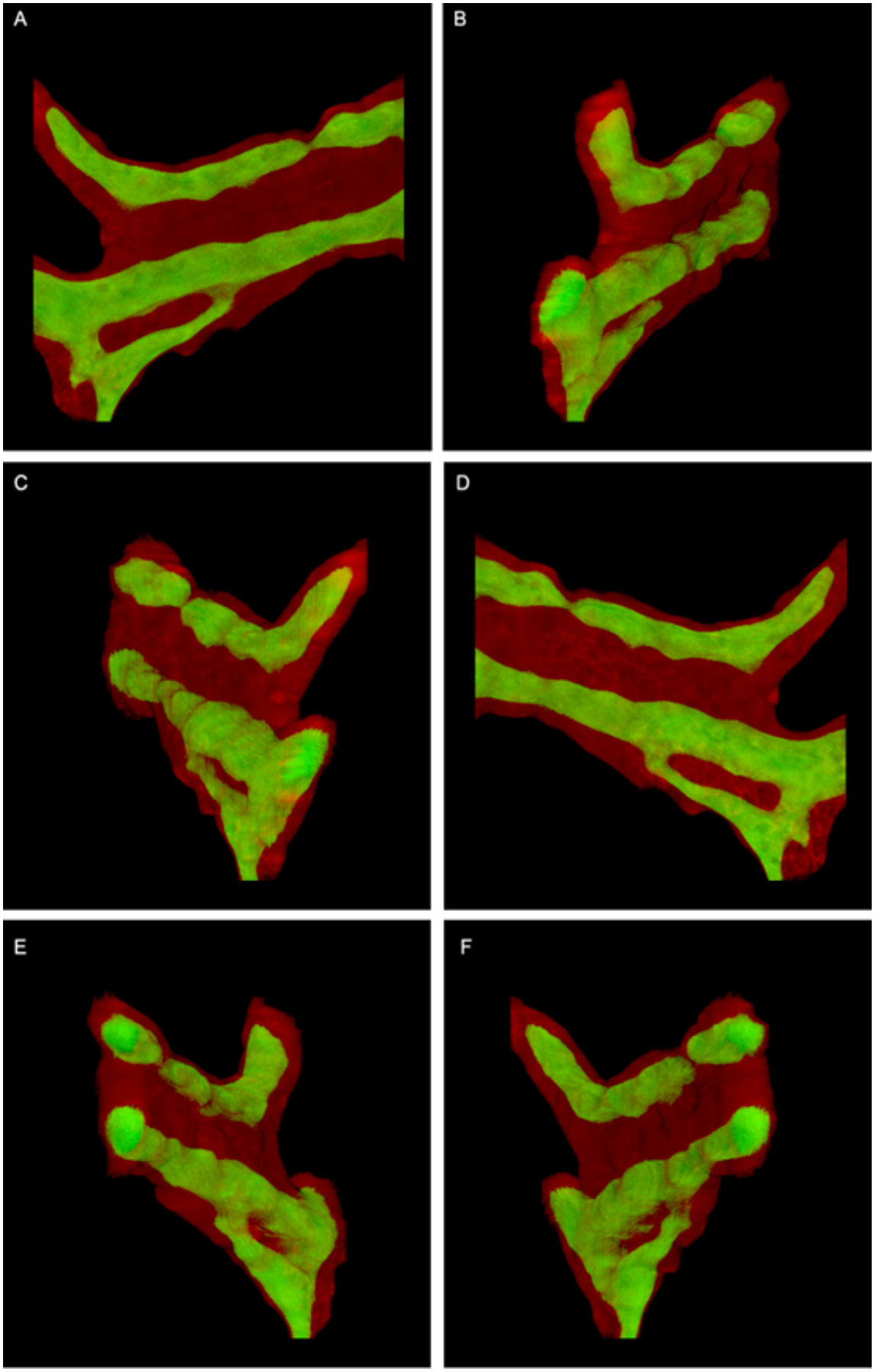
A
B
C
D
E
F

Figure 21. 3D reconstruction of an IV

From a processed image stack single frames of a 360° rotation are shown: (A) 0°, (B) 60° rotated along the azimuth (C) 120°, (D) 180°, (E) 240°, (F) 300°: Viewed in green (FITC-dextran) intravascular space and in red (Rhodamine 6G) the hematopoietic tissue (image size ~250 µm x 250 µm).

4.3 Adoptive Transfer Experiments

After the multidimensional observation by MPM and the spatial analysis of murine skull BM, adoptive transfer experiments using T_{CM} and naïve B-cells were performed for two reasons: first, to explore the capacity of this technique to investigate cell migration and function at a single cell level, and second to ask if there is evidence for a subcompartmentalization of skull BM in terms of cell localization relative to the microvascular segment (for methodology see 3.1.4.3 and 3.2.2).

Figure 22 clearly shows that intravenously injected cells can be identified in the BM region (in this case T_{CM}, but the same is true for naïve B-cells). The left side portrays a simple XY-projection of an image stack. The right side of Figure 22 illustrates a unique feature of intravital MPM: a 3D reconstruction of a processed data set is showing three T_{CM} that reside in the hematopoietic compartment after having left the blood circulation (for methodology see 3.2.4).

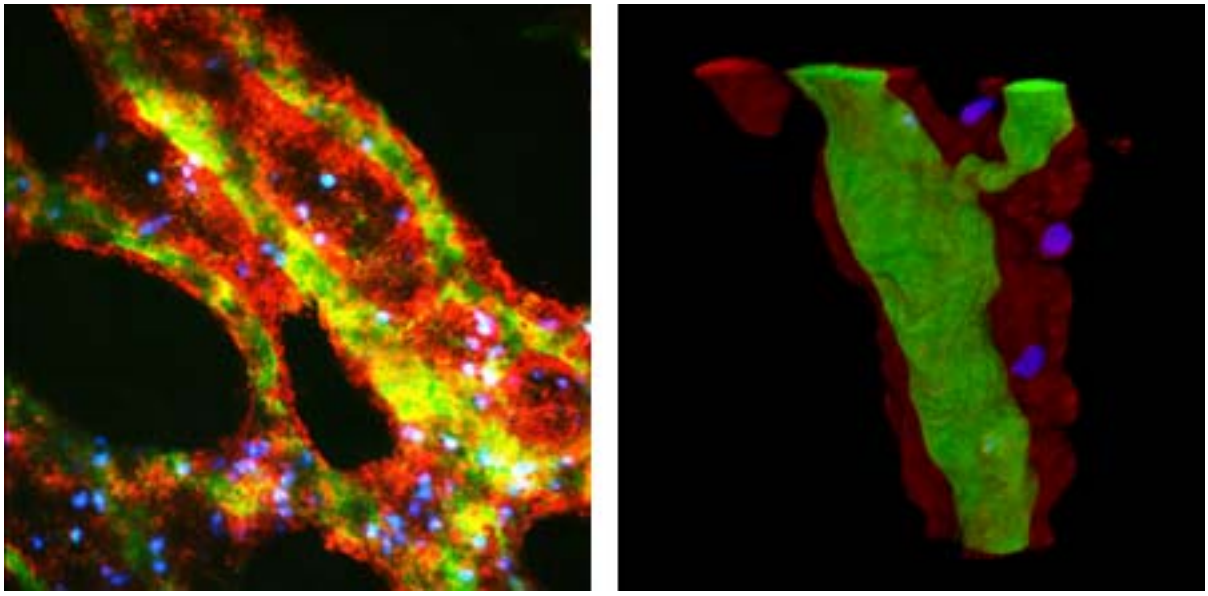

Figure 22. T_{CM} home to the BM compartment

Viewed in green (FITC-dextran) intravascular space, red (Rhodamine 6G) the hematopoietic tissue and homed T_{CM} visualized in blue (Hoechst 33342) 2 hours after injection (left) XY-projection of a raw data image stack (image size 600 µm x 600 µm) (right) 3D-reconstruction of a processed data set rotated ~15°. (image size ~150 µm x 150 µm)

We addressed the question where in the BM cavity injected cells could be found after 2 and 24 hour after injection in relation to the microvessel. Figures 23 and 24 show the results for T_{CM} and naïve B-cells after 2 and 24 hours, respectively.

The distance from the vessel wall to the closest margin of the BM cavity is plotted. This parameter reflects the maximum distance an extravasated cell could migrate away from the microvessel (although it is impossible for the centroid of a cell to reach the outer margin, so the maximum distance should be slightly smaller than the distance to the cavity. In measurements we do not account for this slight difference). On the y-axis the position of a single cell after 2 and 24 hours, respectively, is displayed. Each captured cell is represented as a symbol in the

diagrams. A regression analysis of all cells was blotted as a line. A pink and yellow line are drawn in the diagrams to demonstrate the dimensions of the cavity: the pink line represents the outer border of the cavity, the yellow line represents the middle of the cavity, about half the distance a cell can maximally travel (see above).

Figure 23 shows the diagrams of homed T_{CM} localization in the BM after 2 and 24 hours. After adoptive transfer T_{CM} could be found throughout the BM cavity at both time points homing mainly in cavities with a radius of up to 25 µm around the penetrating vessel. Cavities, whose extravascular radius was broader than ~25 µm, harbored homed T_{CM} mainly in their outer regions. The comparison of the homing pattern after 2 and 24 hours did not yield any statistical significant difference. The slope of the regression line is 0.76 for 2 hour homing and 0.85 for 24 hour homing. Comparing those values to the pink and yellow line (slope of 1.0 and 0.5 respectively) at the time point of 2 and 24 hour after homing, according to the regression line, cells reside between middle and outer margin of the BM cavity.

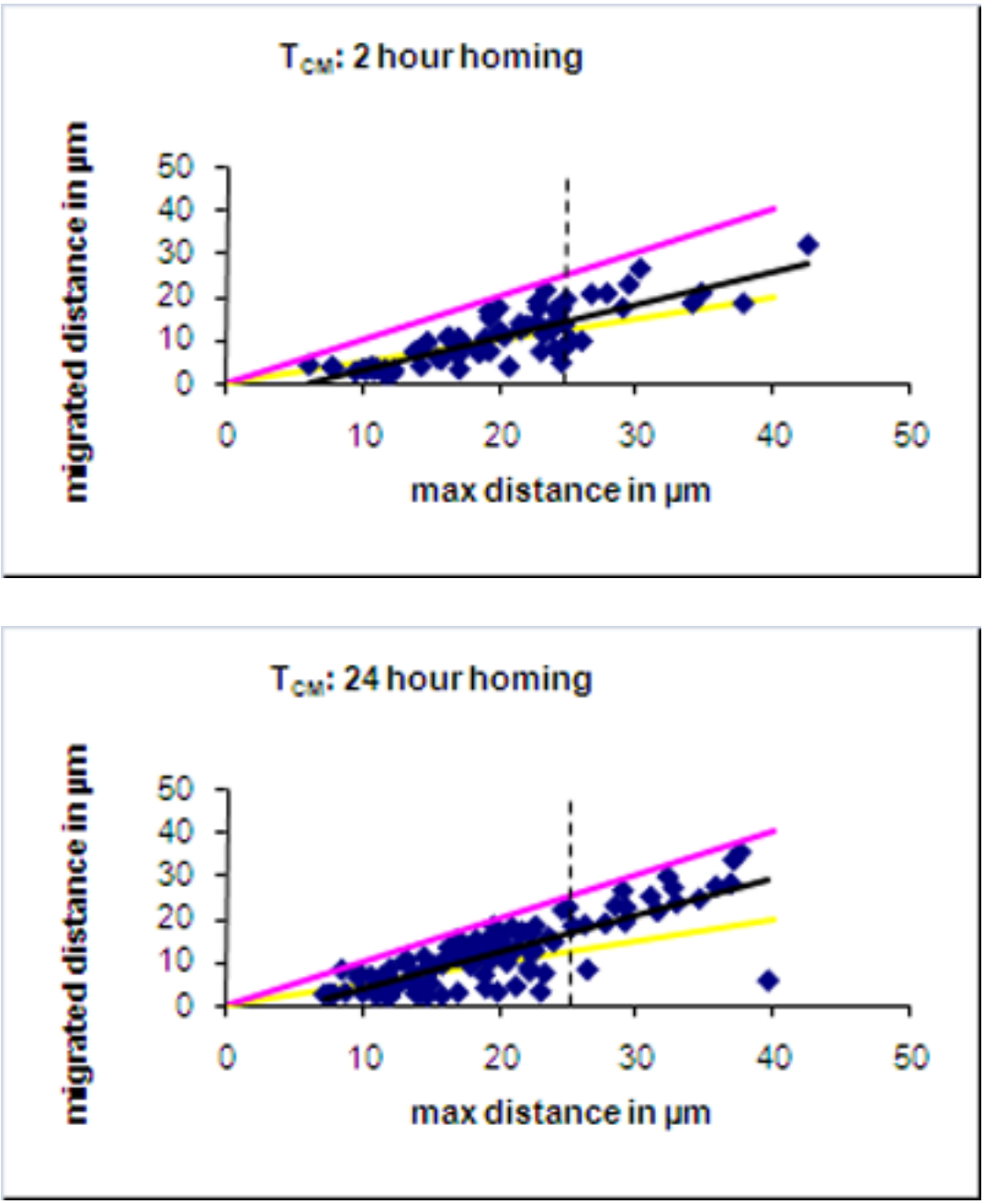

Figure 23. Analysis of T_{CM} homing

(upper panel) 2 hours and (lower panel) 24 hours after injection: One migrated T_{CM} is represented as a blue dot in the diagram, the regression line is shown in black. Pink and yellow lines represent outer boarder and middle of BM cavity respectively. A dotted line illustrates cavity size <25 µm versus >25 µm.

In Figure 24 diagrams of homing studies performed with naïve B-cells after 2 and 24 hours are shown. At both time points naïve B-cells could be found throughout the BM cavity independent of the cavity size. The slope of the regression line is 0.72 for 2 hour homing and 0.77 for 24 hour homing, a non-significant result.

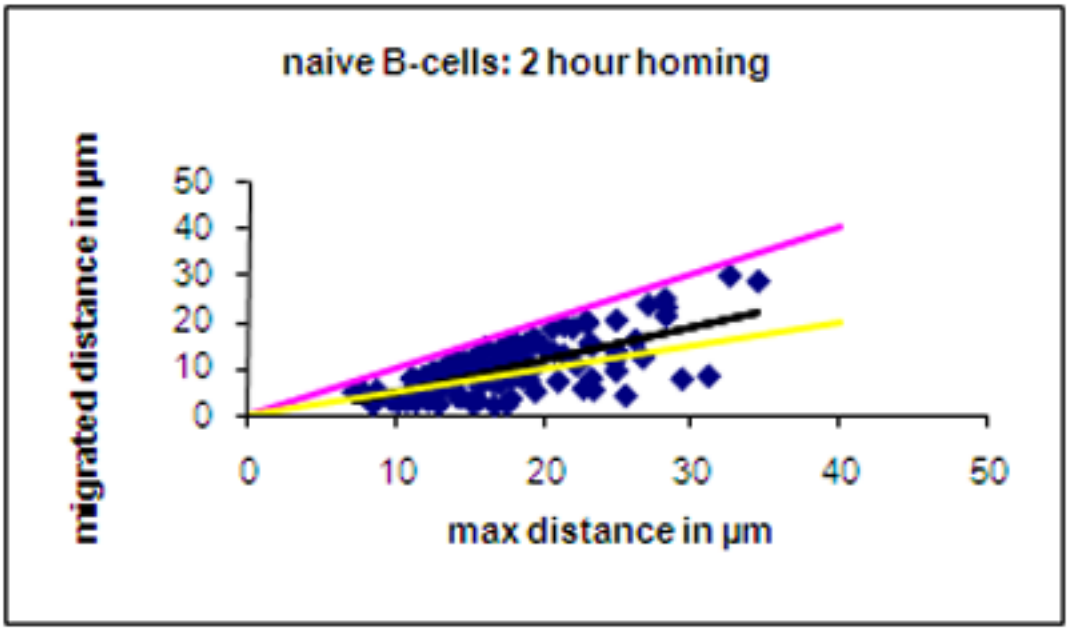

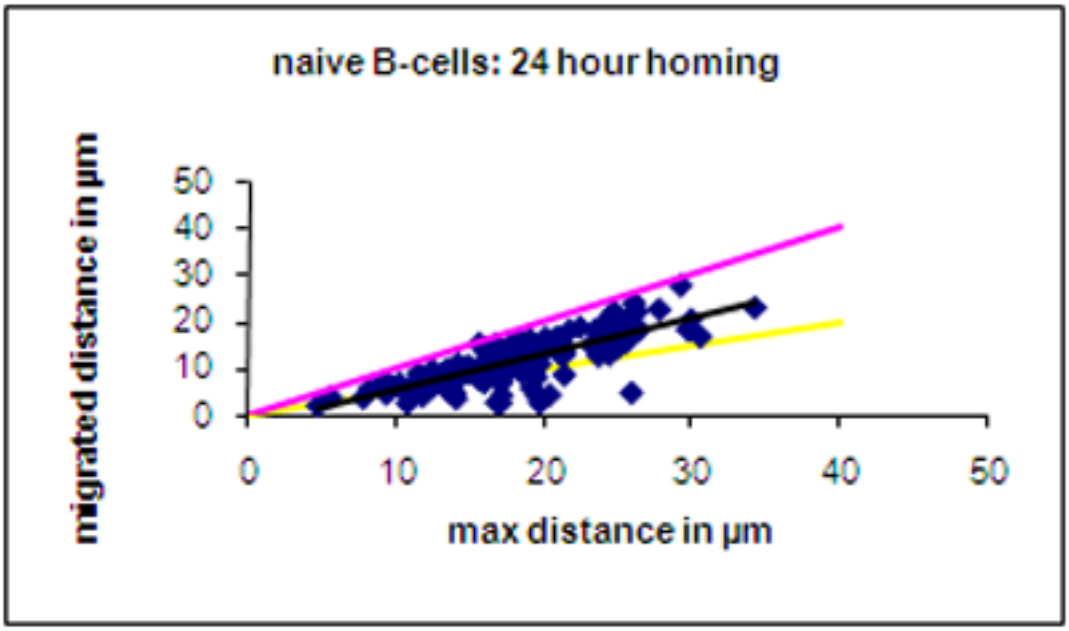

Figure 24. Analysis of naïve B-cell homing

(upper panel) 2 hours and (lower panel) 24 hours after injection: One migrated B-cell is represented as a blue dot in the diagram, the regression line is shown in black. Pink and yellow lines represent outer boarder and middle of BM cavity respectively.

Comparisons of homing pattern after 2 and 24 hour of naïve B-cells and T_{CM} among each other do not show significant differences.

5 Discussion

5.1 Multiphoton Imaging in the Bone Marrow Organ

Multiphoton excitation is based on the physical principle, that a fluorescent dye molecule gets excited by the combined energy of two low energy photons. As outlined in the introduction (see 1.2.1), this fact results in many advantages compared to other fluorescence microscopy techniques, such as CLSM using high energy photons. In the following, we will discuss the advantages and limitations of MPM and give practical examples based on a critical comparison of experimental data acquired using CLSM and MPM in the mouse skull BM model.

One striking advantage is the deeper tissue penetration when using MPM. It is indispensible to use a method that can overcome the anatomic inaccessibility of the BM if this microenvironment should be investigated in its native state despite the surrounding highly scattering compact bone. The comparison of data acquired by CLSM and MPM in equal regions and depth of the BM clearly shows an increase in image contrast and corresponding penetration depth in MPM data sets. Microscope settings for MPM were used as described in 3.1.4.1. Acquisition of confocal data was performed using maximum power of both lasers. No image processing was performed on the data (for methodology see 3.1.4.1). Figure 25 shows a XZ scans (side view) of a CV. Penetration is limited to 75 µm below the bone surface in MPM (upper panel). Looking at the corresponding XZ scan obtained by CLSM (lower panel) the bone tissue cannot be visualized, penetration seems to be equal looking at the staining pattern, but the signal of FITC-dextran and Rhodamine 6G seem fuzzy and that of Rhodamine 6G even less intense. This

can be confirmed looking at XY scans of the same region (Figure 26). Figure 26 shows two XY image sections of the same CV at 2 different depth, 45 µm (left panel) and 65 µm below the bone surface imaged by MPM (top panel) and CLSM (bottom panel). They clearly illustrate that the application of MPM resulted in a higher detection efficiency. The image quality was enhanced compared to CLSM images. MPM images show in-focus images, clear features of vessel and BM region at 45 and 65 µm below the bone surface. On the contrary, confocal images simply show a blurry outline of the imaged feature at 65 µm even more than at 45 µm. In MPM solely emission from the focus spot is detected, forming a clear image, if light is not being scattered too much. Whereas in CLSM also scattered light from out of focus can be detected, possibly giving a fuzzy image (see 1.2.1).

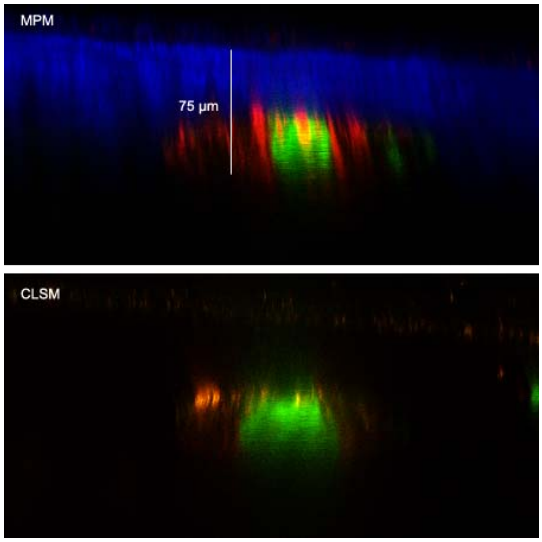

Figure 25. Comparison of MPM and CLSM in XZ images of a CV

side views/XZ scans obtained by MPM (top panel) and CLSM (bottom panel). Green: intravascular space/FITC-dextran staining, red: extravascular space/Rhodamine 6G staining, blue in MPM image: bone tissue/second and third harmonic emission

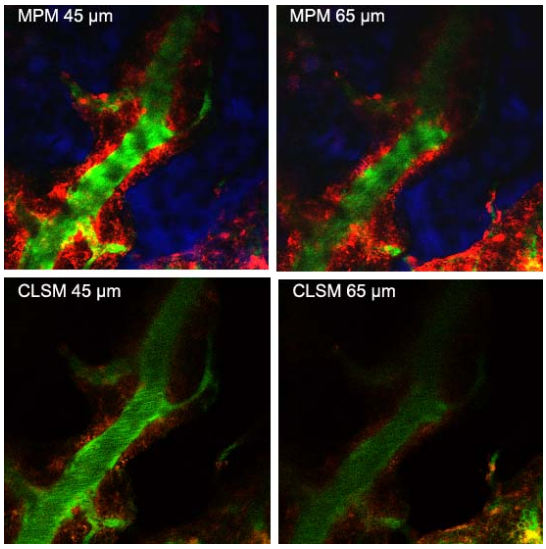

Figure 26. Comparison MPM and CLSM in XY images of a CV

XY scans obtained by MPM (top panel) and CLSM (bottom panel) at 45 µm below the bone surface (left) and 20µm deeper, 65 µm below bone surface (right). Staining see above.

In summary, the tissue penetration of the BM and image resolution offered by MPM are higher. It is possible to collect an image stack, representing a microvascular segment and the surrounding extravascular hematopoietic tissue from top to bottom by MPM, whereas this is impaired in the depth of the BM using CLSM due to deficient information from the depth and blurring by out-of-focus information. High quality images are crucial for quantitative measurements and confocal data was found unfeasible taking this quantitative viewpoint.

In the literature penetration depth by confocal and multiphoton imaging is compared in various media and tissues. Centonze *et al.* presented at least a

twofold improvement in imaging penetration using multiphoton excitation when comparing identical optical sections of different tissues, such as monkey kidneys, cheese, neonatal hamster brain, bovine embryos and beads in a yeast solution, obtained by CLSM and MPM (Centonze and White, 1998). Another study also implicated a significant improvement in penetration depth *in vivo* human skin (Masters et al., 1998).

Although MPM is a very powerful tool it is not without limitations. For example, the frontoparietal part of the skull calvaria is particularly suitable for microscopic visualization because the BM is already macroscopically visible under an extremely thin layer of cortical bone (Mazo et al., 1998). Nevertheless, the practical limit of penetration depth in this study was approximately 75-80 µm (in some cases 100 µm) in multiphoton imaging. The upper panel of figure 27 shows a side view of an IV. Here, the hematopoietic tissue on the bottom of the cavity could be visualized, whereas the bottom of broader vessels, as shown in the lower panel of figure 27, could not be viewed in some areas presumably because the layer of overlying bone tissue was too thick.

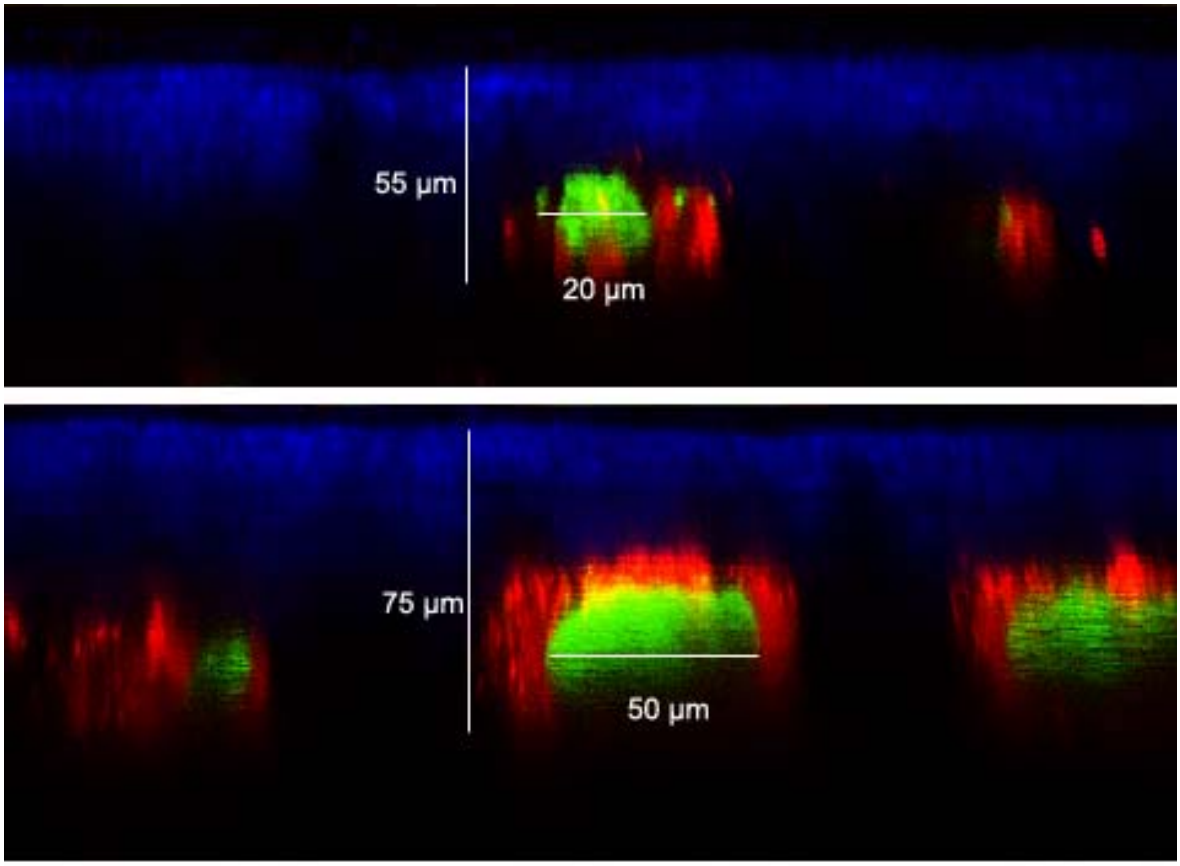

Figure 27. Penetration depth in MPM

In BM regions with smaller vessels the bottom of the BM cavity filled with hematopoietic tissue could be visualized (upper panel). In regions with larger vessels (lower panel) penetration depth was limited and the bottom of the cavity could not be visualized. Green: intravascular space/FITC-dextran staining, red: extravascular space/Rhodamine 6G staining, blue: bone tissue/second and third harmonic emission

Others suggest the possibility of imaging through a layer of 250 µm bone in the mouse skull (Yoder and Kleinfeld, 2002). However, we could not verify these findings in our experimental setup. We tested two tools in the microscope's settings to improve penetration depth on several layers deep within the BM: first, increase of laser power (from 40%, which is used during the entire study, to 90-100%) and second, the "accumulate filter" in image acquisition, which collects

signal over a longer period of time. We compared this acquired data with corresponding data acquired with standardized original microscope settings that were used throughout the study. We could neither detect any increase in penetration depth nor an enhancement of image quality (data not shown). Recent advances in laser technology may allow deeper tissue penetration.

Our attempts to obtain in-focus images from deeper tissue remained unsuccessfully. Only a marginal increase in imaging depth could be accomplished. Probably light was being scattered too much, preventing the formation of any focus spot. We circumvented these difficulties by adapting our analysis procedures, when visualizing the bottom of the BM cavity was impaired, such as in regions of vessels with a large diameter - CV or PSV. These were analyzed and quantified in a different way based on the assumption of geometric symmetry of the upper and lower halves of the BM cavities, when XZ scans did not show the bottom of the cavity. 3D-reconstruction of small microvessels with surrounding BM give evidence of geometric symmetry (see Figures 21 and 22). In case of impaired viewing in deeper parts, the largest vessel diameter in the horizontal plane indicated the center of the vessel. The volumes of intra- and extravascular BM space in and around the top half of the vessel were counted and multiplied by two. This approach allowed us to generate a reasonable estimate of the volume of intra- and especially extravascular space deep within in the bone tissue.

Multiphoton excitation offers several advantages in terms of utilization of fluorophores. In MPM, multifluorophore excitation, meaning the excitation of different fluorophores by one single laser source, becomes possible (Xu et al., 1996). In this study three applied fluorophores, FITC-dextran, Rhodamine 6G and Hoechst 33342 could be excited by the same excitation wavelength of 800 nm.

Moreover, the bone tissue could be visualized without specific labeling. The multiphoton illumination induces second or third harmonic generation in certain biological structures (Christie et al., 2001; Friedl et al., 2007), which proved to be useful to our application as seen in Figure 25 and 26. We found that by multiphoton imaging this second and third harmonic emission, together with UV excited autofluorescence, from the bone tissue located the bony BM cavity without the application of external fluorophores. Using CLSM, fluorescent dyes are needed to visualize all features, including the bone tissue. Recently, the use of intrinsic fluorescence and second and third harmonic generation has been intensively studied and is likely to contribute to the application of MPM in the future, because external labeling of various structures and molecules is unfeasible (Campagnola et al., 1999; Zipfel et al., 2003).

Another remaining critical issue is image distortion in the Z-axis. This phenomenon is often induced by refractive index mismatches between the sample and the imaging medium (Hell et al., 1993; Leung, 1993; Sheppard and Torok, 1997). To minimize measurement errors due to this effect, a water immersion objective was used throughout the experiments. We chose the dipping type which permits direct imaging of the skull BM area through a pool of physiologic saline. These lenses (40 x WI: NA 0.8, 10 x WI: NA 0.3), had a working distance, long enough to focus through most of the BM areas. Recently, new Olympus a 20 x WI, 0.95 NA and 60 x WI, 1.2 NA water immersion lenses are used by our group, but no comparison in terms of improved image quality in terms of depth and distortion has been done so far.

There have been attempts to correct for refractive index mismatch induced distortion in confocal and MPM based on simplified biological samples or beads

(Booth and Wilson, 2000; Bucher et al., 2000; Neil et al., 2000; Sherman et al., 2002). However, when investigating a complex and bony, heterogeneous *in vivo* microenvironment, such as the BM, attempts to restore and correct for such optical aberrations have remained complicated (Diaspro et al., 2002). We dealt with the problem of distortion in various simplified experiments using fluorescently labeled beads of different diameters that we introduced into the bone tissue. Comparing the degree of distortion could not identify a clear difference. Nevertheless, this attempt of quantifying distortion imaging the BM organ could not give definite answers to this problem (data not shown). It must also be considered that the distortion potentially affecting the actual measurements of tissues underneath the bone, would only minimally affect the ratios between different compartments in the same tissue because fluorescent signals from these areas would have suffered a comparable amount of distortion. Therefore, we chose to quantify wherever possible the spatial relationships of the intra- and extravascular compartment as ratios rather than absolute volumes.

However, disregarding the remaining limitations in MPM, the examination of the difference between CLSM and MPM according to the performance in the BM organ indicates the power of multiphoton excitation that cannot be surpassed by any other technique *in vivo* so far.

5.2 Experimental Design of the Study

Several factors are crucial to analyze spatial relationships in the BM environment. First, regions of interest have to be effectively delineated, second, the animal itself and third, the microscope settings may entail certain variables that could alter

results to some extent. In the following paragraph these factors are individually discussed.

Spatial information of intra- and extravascular compartments was based on fluorescent labeling of these areas and therefore depended on the exact staining characteristics of fluorophores. To contrast the two BM compartments, the intravascular space and the surrounding extravascular space, FITC-dextran and Rhodamine 6G were administered respectively (for methodology see 3.1.2.2). FITC-dextran (168 kD MW) is an inert plasma marker that remains confined to the vessel lumen and is useful to delineate the intravascular space (von Andrian, 1996). It is broadly used to view microvasculature in intravital microscopy techniques and has been effectively applied to quantitative analysis of certain microvasculature before (Brunner et al., 2000; Tyrrell et al., 2005). Low-molecular-weight Rhodamine 6G mainly stains mitochondria (Johnson et al., 1981) and therefore should stain conglomerations of metabolically active cells, hence the extravascular space that is filled with hematopoietic tissue. Mazo *et al.* found that after Rhodamine 6G injection, a typical staining pattern of the extravascular BM compartment could be observed, which was unique to the skull calvaria and could not be seen in other tissues (Mazo et al., 1998). Ever since, Rhodamine 6G has been used in various studies of our group demarcate the BM compartment (Mazo and Von Andrian, 1999; Mazo et al., 2002; Cavanagh et al., 2005; Mazo et al., 2005).

To further illustrate the property of these two fluorophores to exactly stain the intra- and extravascular compartment, figure 28 shows an example of fluorescence distribution in the region of a branched IV. Rhodamine 6G stained hematopoietic tissue within the BM cavity (upper left panel) and FITC-dextran delineated the

intravascular space (upper right panel). Since the hematopoietic tissue is surrounded by bone, which is not stained by Rhodamine 6G, a negative outline of the cavity could easily be identified with the Rhodamine 6G contrasting technique. Since multiphoton excitation is capable of obtaining the combined second and third harmonic emission and UV excited autofluorescence from the bone tissue, it was possible to indentify a positive outline of the BM cavity, which can be seen in the lower left panel. Looking at the merged image of all three channels (lower right panel), it becomes clear that the negative and positive outlines of the cavity given by the contrasting techniques form a uniform border. The same is true for the outline of the microvasculature, which is viewed by direct FITC-dextran staining and indirectly by the Rhodamine 6G distribution (Figure 28).

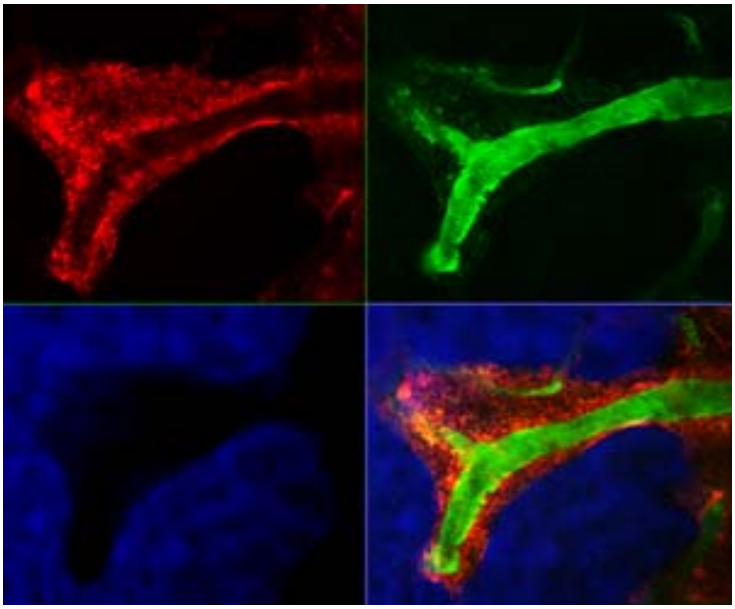

Figure 28. Fluorescence distribution in a BM cavity

Upper left panel shows in red the Rhodamine 6G distribution, staining leukocytes in the intra- and, especially, extravascular space, in the upper right panel FITC-dextran delineating the intravascular space shows in green, the lower left panel demonstrates the bone tissue in blue by second and third harmonic emission, a positive outline of the BM cavity and in the lower right panel the merged image. (Settings of the microscope system are outlined in 3.1.4.1)

The two compartments within the bone tissue, the intravascular space and the surrounding densely packed hematopoietic tissue, forming the extravascular space of the BM microenvironment in the mouse skull are reasonably well delineated by these fluorophores. Consequently, the pattern of fluorescent labeling of these two compartments is unlikely to alter the quantitative view.

During image collection individuality of the animal may serve as source of error. An exceptional thick layer of bone as highly scattering tissue could impair the view deep within tissue and affect the quality and intensity value of the image. An adequate blood circulation is also obligatory for a uniform distribution of

fluorophores, whereas irregular stainings of intra- and extravascular BM space could be rarely caused by a poor circulation due to surgical or anesthesiological techniques. Particular areas of well defined, uniformly stained vessels under a relatively thin layer of bone were chosen for analysis to avoid these confounding factors. Furthermore, FITC-dextran can extravasate to a larger extent across vascular walls with a highly irregular basement membrane. This could result in a misleading extravascular signal.

BM microvessels may contain adherent leukocytes, which are stained with Rhodamine 6G. These could affect the accuracy where vessel boundaries have been defined by the FITC-dextran distribution. If those regions were not already excluded from measurements, in most cases these deficiencies could be remedied by setting intensity thresholds during image processing.

For reliable quantitative measurements the microscope's settings during image acquisition are the third crucial factor: The imaging system's settings, such as laser power, gain and offset are critical parameters, since saturating high intensity levels are known to induce measurement errors in laser scanning microscopy (Leung and Jeun, 1992). Therefore, proper adjustments of these settings are essential to minimize over-saturation of image intensities. We found that after the optimal levels of adjustments had been determined the same settings could be applied to our experiments, yielding a set of relatively standardized image collection parameters.

In summary, we minimize possible variables during data acquisition that could have an impact on our conclusion regarding spatial relationships in the BM (for methodology see 3.1.4).

Potential variables that could have affected the results in adoptive transfer experiments are best discussed in connection with the results itself, and are therefore further outlined in chapter 5.5.

5.3 Image Processing and Analysis

The 3D visualization and measurement software VoxBlast was used in all of the quantification measurements. This software allows the automatic tracing of a 3D volume (Z-series image stack) section by section. However, for VoxBlast to perform such a measurement routine, one must first isolate the measurement area as AOI. Unfortunately, we found that VoxBlast was deficient in isolating well defined AOI from most of our raw data image stacks especially those containing weakly stained venules or those that were collected at deeper parts of the BM. On the other hand, we found that the graphics software Photoshop worked very well in this respect. Therefore, we used Photoshop to isolate AOI, representing intravascular or extravascular volume on each image, before exporting them back to VoxBlast for measurement and analysis. An intensity threshold of 20-25 (excluding grayscale value of 0 to 20-25) was applied to all of the images so that regions with the intensity below this value (typically background fluorescence) were excluded from the measurements. This approach selected intravascular regions and the total BM compartment into well defined AOIs and the results were highly reproducible. A macro (called “action” in Photoshop) was used to automate the task so that venule and BM regions of a Z-series image stack were delineated with a single mouse click, avoiding more time consuming image processing. Images of venules and the surrounding BM compartments thus isolated exhibit a

well defined 3D morphology (Figure 21 and 22) (for methodology see 3.2.1).

The design of our measurement protocol hinges upon the accuracy of delineating venule and BM regions. In this study a thresholding technique was used for this purpose. Image thresholding is used in various fields: To monitor disease activity of multiple sclerosis e.g., image processing on MRI (magnetic resonance tomography) data utilizes thresholding to quantify lesions in the central nervous system (Grimaud et al., 1996; Achiron et al., 2002). An osteoporosis study has used a thresholding technique on MRI and microcomputed tomography data of the radius (Pothuaud et al., 2002). The analysis of angiogenic vasculature is a broad field, e.g. in tumorigenesis and -therapy, and necessitates vessel tracing methods, that amongst others, use thresholding based on intensity values, as reviewed by Abdul-Karim *et al.* (Abdul-Karim et al., 2003a; Abdul-Karim et al., 2003b). Ranefall *et al.* provide an automatic approach to quantify microvessels using dynamic thresholding of the average component size histogram (Ranefall et al., 1998). Thresholding based on grayscale level is referred to as one of the most popular and efficient methods for image processing by Kim *et al.* and is used to quantify carotid artery stenosis on MRI data (Kim and Park, 2004). Umesh Adiga *et al.* outline simple but efficient techniques to enhance visual quality in confocal microscopy data, also partly by the application of thresholding (Umesh Adiga and Chaudhuri, 2001). Another field worth mentioning is neuroscience: to reveal the 3D neural morphology sophisticated techniques of image utilization and processing are needed. Wearne *et al.* summarize the current techniques, involving thresholding as well, to gain insight into the global neuronal morphology (Wearne et al., 2005). The few studies described in this paragraph should exemplify on one hand the broad application and necessity of image processing and thresholding

and on the other hand illustrate its utility across diverse disciplines. Nevertheless, experimental setup, data acquisition and parameters that express results differ from study to study. Therefore, it cannot be assumed that image processing has to be performed in a generalized way. In fact, each study requires an individual approach of image processing for optimal results. In this study, using an intensity threshold of 20-25 (excluding all grayscale values from 0 to 20-25) to isolate BM and vessel regions was prompted by our successful, but time-consuming initial attempt to manually trace the AOI by hand. We found that venule and BM regions isolated using these threshold values matched closely with those from manual tracings and also limited subjective input and observer bias, especially where boundaries could not be clearly identified. In all of our experiments, a fixed value between 20 to 25 (grayscale value) was applied to the entire Z-series image stack. Variability of 5 grayscale values was allowed to choose the subjectively best delineation of AOI by thresholding. The discrepancy of measurement results between using a value of 20 to that of 25 was approximately 3-10% (based on calculations made on identical Z-stacks). Using a Photoshop “action” to automate the steps also help eliminate further subjective input and potential user error. In addition, the described thresholding technique has the advantage to compensate for images collected under less than ideal conditions as mentioned above.

Adobe Photoshop has been designed and marketed as a photo-editing software used mainly by photographers and graphics artists. In medicine, this software has been recommended by several radiologists for image presentation (Caruso and Postel, 2002; Corl et al., 2002). The use of this software by many microscopists has been largely limited to the assembly of micrographs into “plates” in preparation for journal publication. However, this software has many sophisticated features

that are useful to microscopists, such as merging of color channels from digital images of fluorescence microscopy and performing simple 3D reconstruction tasks from image stacks. Furthermore, it has been previously used for image analysis (Lehr et al., 1997; Lehr et al., 1999; Vilaplana and Lavialle, 1999; O'Shaughnessy and Fitzgerald, 2000; Schnapper et al., 2002; Mofidi et al., 2003; Kirkeby and Thomsen, 2005; Sugawara et al., 2005). In addition, Photoshop has been lately referred to as a versatile tool with a wide range of potential applications in microcirculation research (Brunner et al., 2000). Here, we used this software to obtain reproducible and objective quantitative measurements.

In summary, the image processing technique individually created for this study using Adobe Photoshop, is found to be very practical to highlight AOI and eliminate background noise, as well as compensating for irregularities acquired during image collection.

5.4 Spatial Relationships in the Bone Marrow

In this study the relative spatial distribution of FITC-dextran as a marker for the intravascular space of the BM compartment and Rhodamine 6G, labeling hematopoietic tissue / the extravascular space was compared for five different microvascular segments (for methodology see 3.2.1). The results show that small vessels with a diameter of ~25 µm, such as IV, S and vessels of the CN are surrounded by relatively larger conglomerations of hematopoietic cells than vessels with a greater diameter of ~60 µm, such as CV and PSV (for detailed results see chapter 4.2).

There are various reasons that could explain these findings and should be further

discussed. First, the relative amount of hematopoietic tissue appears to be related to the diameter of the vessel which penetrates the cavity. According to the vessel diameter, hemodynamic parameters, such as blood and cell velocity and wall shear rate can differ. Mazo *et al.* e.g. measured a lower blood velocity, red blood cell velocity and wall shear rate for small-sized IV compared to greater vessels, such as CV and PSV (Mazo et al., 1998; Mazo and Von Andrian, 1999). These hemodynamic conditions in smaller microvessels likely facilitate extravasation and homing of various cells and therefore could account for the greater accumulation of hematopoietic cells in these microvascular segments compared to large-sized vessels.

Second, the different levels of the microvascular segments in the blood circulation have to be considered. Blood flow is directed from IV and S to the CV, in case of S frequently via a PSV, leading to differences in the oxygen tension. Since S and IV are perfused first, the oxygen concentration in these areas is presumably higher compared to downstream segments, such as CV and PSV. Therefore, extravascular cell accumulation could be relatively enriched around IV and S, due to better gas exchange in these areas. In general, the oxygen supply could define the maximum capacity and dimensions of the extravascular compartment. Of course, a microenvironment for immunological activity requires not only an adequate gas exchange, but also its size could be influenced by various other factors, such as chemokine- and growth factor distribution.

As discussed above, we have focused on the relative spatial distribution of hematopoietic tissue and not on the absolute volume, since our capacity for accurate measurements of total volumes is limited. Therefore, no direct conclusion can be drawn: the absolute volume of the hematopoietic tissue could be the same

for all microvascular segments, or even greater around larger vessels.

5.5 Subcompartmentalization of the Bone Marrow

As outlined in the introduction, it has been reported that the spatial localization of different subpopulations of cells in the BM compartment varies in terms of central- or endosteal marrow region according to their stage of development and maturity: migration is believed to be directed from the outer part of the cavity towards the central region with cell maturation (Hermans et al., 1989; Jacobsen and Osmond, 1990; Calvi et al., 2003). Accordingly, hematopoietic progenitors preferentially reside in the outer regions of the BM cavity (Lord et al., 1975; Nilsson et al., 2001; Calvi et al., 2003; Zhang et al., 2003). We addressed the question whether naïve B-cells as a representative of a fully differentiated, immunologically naïve cell population and T_{CM} representing a mature memory type cell population have a special localization in the hematopoietic compartment which surrounds a single BM vessel (for methodology see 3.2.2). It has been previously shown, that both cell types home to the BM (Berlin-Rufenach et al., 1999; Di Rosa and Santoni, 2003). However, it was unclear, whether B-cells freely recirculate or stay in the extravascular part of the BM as a sessile population. Also, the localization of T_{CM} within the BM after homing was not described. Therefore, we compared the position of the two cell populations after 2 and 24 hour homing in the IV and S region. We expected to find the memory type cell population close to the endothelium, in a waiting position, to be rapidly released into the circulation when needed in certain sites of immunological reactions. Do naïve B-cells take a particular position in respect to a BM microvessel?

Both cell populations, T_{CM} and naïve B-cells were found in the extravascular region of the BM cavity after 2 and 24 hour homing. Apparently, there is no predefined region in terms of distance to a BM microvessel, where B-cells and T_{CM} do not localize. The slopes of regression lines did not show any significant difference according to time point and cell type. Values of slopes differed between 0.72 and 0.85, meaning that the mean position between the migrated cell and the vessel wall at the investigation time point was situated in the outer half of the cavity. Looking at the distribution of single cells no preference of position was evident. Only single T_{CM} in large-sized cavities up to 40 µm seemed to reside preferentially close to the endosteal tissue (for detailed results see 4.3).

From a static view of individual BM regions single cells could be seen at any position on a virtual line between the vessel and the outer boarder of the BM cavity at both time points. In this experimental setup the evidence for T_{CM} to reside close to the vessel wall cannot be confirmed. Also, an explicit location of naïve B-cells in terms of relation to BM microvessel cannot be drawn from this experiment.

Since the investigation is based on static images the position of the cell simply represents a snapshot in a possible continuous sequence of positions the cell might take since a single cell was not followed over time. Also, results are based on XZ-scans of single migrated cells that were subjectively chosen according to image quality. Fluorescence distribution and vessel situation might neither reflect a random selection of cells nor is a view on groups of cells allowed. Looking at cell motility is proved to be crucial to make further conclusions on localization of cell populations in the BM. In summary, our adoptive transfer experiments show that MPM in general is a suitable tool to investigate at the single cell level. Nevertheless, conclusions on the subcompartmentalization of the BM region

demand continuous investigation of cells over time on a single cell basis as well as observing the relationship between cells in the BM compartment.

Meanwhile our group continuously observed cell migration and found that T_{CM} are highly motile (6.5 µm/min., SEM 0.2) and migrate over long distances random in direction, although cells likely preferred moving close to venules and sinusoids (Mazo et al., 2005). Consistent with this, another study of our group found that antigen-bearing dendritic cells migrate to the BM to present antigen to resident T_{CM} (Cavanagh et al., 2005). For B-cells as well, it has been recently reported that certain cellular niches can be identified depending on B-cell maturity (Tokoyoda et al., 2004). Cariappa *et al.* reveal an extravascular perisinusoidal niche for mature B-cells neighboring in clusters observing B-cells over time (Cariappa et al., 2005).

6 Summary

The BM is a key organ of hematopoiesis and also has an important role in the immune system. The BM microenvironment is a complex, highly vascularized 3D structure composed of different cell types and extracellular matrix. Intense cellular traffic takes place from the peripheral blood to the BM and vice versa. However, the precise arrangement and microscopic dimensions of this environment have only been inferred so far from static imaging of sectioned tissue. We developed a new model to characterize and analyze the 3D microanatomy of murine skull BM in its physiological state using intravital MPM. This technology offers deep tissue penetration, low phototoxicity, superior image contrast and 3D resolution compared to other microscopy techniques. This makes MPM a powerful tool to investigate the BM, overcoming its anatomic inaccessibility. To quantify the dimensions of the BM compartment, we used high molecular weight FITC-dextran and Rhodamine 6G, which delineated the intra- and extravascular space, respectively. Measurements were generated using the 3D visualization and measurement software VoxBlast 3.1 after using a thresholding technique carried out by Adobe Photoshop 6.0. Results were expressed as the ratio of intravascular to extravascular space for different microvascular segments. Moreover, we performed adoptive transfer experiments with isolated naïve B-cells and T_{CM} and studied their location within the BM compartment. The new approach presented here will be a useful tool for further *in vivo* investigations of cell behavior, trafficking and interactions in the BM.

7 Zusammenfassung

Das Knochenmark übernimmt eine Schlüsselfunktion in der Hämatopoese und hat eine wichtige Rolle im Immunsystem. Das Organ besteht aus einer hoch vaskularisierten 3D Struktur, die sich aus unterschiedlichen Zelltypen und einer extrazellulären Matrix zusammensetzt. Ständige Zellmigration erfolgt vom peripheren Blut in das Knochenmark und vice versa. Allerdings lassen sich das genaue Arrangement und die mikroskopischen Dimensionen dieses Organs bisher nur durch statische Bildgebung von geschnittenem Gewebe ableiten. Wir haben ein neues Modell entwickelt, um die 3D Anatomie des Knochenmarks im Mausschädel mit Hilfe intravitaler MPM in physiologischem Zustand zu charakterisieren und zu analysieren. Im Vergleich zu anderen Mikroskoptechniken ermöglicht diese Technik eine hohe Eindringtiefe, geringe Phototoxizität, gehobenen Bildkontrast und 3D Auflösung. Diese Eigenschaften machen MPM zu einem äußerst nützlichen Instrument, um das sonst unzugängliche Knochenmark zu untersuchen. Wir haben hochmolekulares FITC-Dextran und Rhodamine 6G benutzt, um den intra- bzw. extravaskulären Raum zu kennzeichnen und darauf basierend die Dimensionen dieser beiden Kompartimente zu analysieren. Messungen wurden nach der Anwendung einer Bildverarbeitungstechnik in Adobe Photoshop 6.0 durch die 3D-Visualisierungs- und Vermessungssoftware VoxBlast 3.1 vorgenommen. Die Resultate wurden als Quotient von intravaskulärem zu extravaskulärem Raum für unterschiedliche vaskuläre Segmente dargestellt. Darüberhinaus haben wir “adoptive transfer”- Experimente mit naiven B-Zellen und T_{CM} durchgeführt, und haben deren Lokalisation im Knochenmarksraum

untersucht. Die hier präsentierte neue Herangehensweise wird für die weitere Erforschung von *in vivo* Verhalten, Migration und Interaktionen von Zellen im Knochenmark überaus nützlich sein.

8 References

Abdul-Karim, M., Al-Kofahi, K., Brown, E.B., Jain, R.K. and Roysam, B. (2003a) Automated Tracing and Change Analysis of Angiogenic Vasculature from in vivo Multiphoton Confocal Image Time Series. Microvasc Res 66, 113-25.

Abdul-Karim, M., Al-Kofahi, O., Brown, E., Jain, R., Al-Kofahi, K. and Roysam, B. (2003b) Automated in vivo change analysis of tumor vasculature from two-photon confocal image time series. Multiphoton Microscopy in the Biomedical Sciences III 4963, 151-159.

Achiron, A., Gicquel, S., Miron, S. and Faibel, M. (2002) Brain MRI lesion load quantification in multiple sclerosis: a comparison between automated multispectral and semi-automated thresholding computer-assisted techniques. Magnetic Resonance Imaging 20, 713-720.

Bajenoff, M., Egen, J.G., Koo, L.Y., Laugier, J.P., Brau, F., Glaichenhaus, N. and Germain, R.N. (2006) Stromal cell networks regulate lymphocyte entry, migration, and territoriality in lymph nodes. Immunity 25, 989-1001.

Bajenoff, M. and Germain, R.N. (2007) Seeing is believing: a focus on the contribution of microscopic imaging to our understanding of immune system function. Eur J Immunol 37 Suppl 1, S18-33.

Becker, M.D., Nobiling, R., Planck, S.R. and Rosenbaum, J.T. (2000) Digital video-imaging of leukocyte migration in the iris: intravital microscopy in a physiological model during the onset of endotoxin-induced uveitis. J Immunol Methods 240, 23-37.

Beltman, J., Maree, A., Lynch, J., Miller, M. and de Boer, R. (2007) Lymph node topology dictates T cell migration behavior. J. Exp. Med. 204, 771-780.

Berlin-Rufenach, C., Otto, F., Mathies, M., Westermann, J., Owen, M.J., Hamann, A. and Hogg, N. (1999) Lymphocyte Migration in Lymphocyte Function-associated Antigen (LFA)-1-deficient Mice. J. Exp. Med. 189, 1467-1478.

Biorad Laboratories. (Hemel Hempstead, UK) www.cellscience.bio-rad.com.

Bolch, W., Patton, P., Rajon, D., Shah, A., Jokisch, D. and Inglis, B. (2002) Considerations of Marrow Cellularity in 3-Dimensional Dosimetric Models of the Trabecular Skeleton. J Nucl Med 43, 97-108.

Booth, M.J. and Wilson, T. (2000) Strategies for the compensation of specimen-induced spherical aberration in confocal microscopy of skin. J Microsc 200 (Pt 1), 68-74.

Bousso, P., Bhakta, N.R., Lewis, R.S. and Robey, E. (2002) Dynamics of Thymocyte-Stromal Cell Interactions Visualized by Two-Photon Microscopy. Science 296, 1876-1880.

Bousso, P. and Robey, E. (2003) Dynamics of CD8+ T cell priming by dendritic cells in intact lymph nodes 4, 579-585.

Branemark, P. (1959) Vital mircroscopy of bone marrow in rabbit. Scand J Clin Lab Invest. 11 (Supp 38), 1-82.

Brown, E., Campbell, R., Tsuzuki, Y., Xu, L., Carmeliet, P., Fukumura, D. and Jain, R. (2001) In vivo measurements of gene expression, angiogenesis and physiological function in tumors using multi-photon laser scanning microscopy. Nat Med 7, 864-868.

Brunner, J., Krummenauer, F. and Lehr, H.A. (2000) Quantification of video-taped images in microcirculation research using inexpensive imaging software (Adobe Photoshop). Microcirculation 7, 103-7.

Bucher, D., Scholz, M., Stetter, M., Obermayer, K. and Pfluger, H.J. (2000) Correction methods for three-dimensional reconstructions from confocal images: I. Tissue shrinking and axial scaling. J Neurosci Methods 100, 135-43.

Cahalan, M. and Parker, I. (2006) Imaging the choreography of lymphocyte trafficking and the immune response. Curr Opin Immunol. 18, 476-82.

Cahalan, M.D., Parker, I., Wei, S.H. and Miller, M.J. (2002) Two-photon tissue imaging: seeing the immune system in a fresh light. Nat Rev Immunol 2, 872-80.

Calvi, L., Adams, G., Weibrecht, K., Weber, J., Olson, D., Knight, M., Martin, R., Schipani, E., Divieti, P., Bringhurst, F., Milner, L., Kronenberg, H. and Scadden, D. (2003) Osteoblastic cells regulate the haematopoietic stem cell niche. Nature 425, 841-846.

Campagnola, P.J., Wei, M.-d., Lewis, A. and Loew, L.M. (1999) High-Resolution Nonlinear Optical Imaging of Live Cells by Second Harmonic Generation. Biophys. J. 77, 3341-3349.

Carballido, J.M., Biedermann, T., Schwarzler, C. and de Vries, J.E. (2003) The SCID-hu Skin mouse as a model to investigate selective chemokine mediated homing of human T-lymphocytes to the skin in vivo. Journal of Immunological Methods 273, 125-135.

Cariappa, A., Mazo, I., Chase, C., Ning Shi, H., Liu, H., Li, Q., Rose, H., Leung, H., Cherayil, B., Russell, P. and Von Andrian, U.H. (2005) Perisinusoidal B Cells in the Bone Marrow Participate in T-Independent Responses to Blood-Borne Microbes. Immunity 23, 397-407.

Carrasco, Y. and Batista, F. (2007) B cells acquire particulate antigen in a macrophage-rich area at the boundary between the follicle and the subcapsular sinus of the lymph node. Immunity 27, 160-71.

Caruso, R. and Postel, G. (2002) Image Editing with Adobe Photoshop 6.0. Radiographics 22, 993-1002.

Cavanagh, L.L., Bonasio, R., Mazo, I.B., Halin, C., Cheng, G., van der Velden, A.W.M., Cariappa, A., Chase, C., Russell, P., Starnbach, M.N., Koni, P.A., Pillai, S., Weninger, W. and von Andrian, U.H. (2005) Activation of bone marrow-resident memory T cells by circulating, antigen-bearing dendritic cells 6, 1029-1037.

Cavanagh, L.L. and Weninger, W. (2008) Dendritic cell behaviour in vivo: lessons learned from intravital two-photon microscopy 86, 428-438.

Celli, S. and Bousso, P. (2007) Intravital two-photon imaging of T-cell priming and

tolerance in the lymph node. Methods Mol Biol. 380, 355-63.

Celli, S., Breart, B. and Bousso, P. (2008) Intravital Two-Photon Imaging of Natural Killer Cells and Dendritic Cells in Lymph Nodes. Methods Mol Biol. 415, 119-126.

Celli, S., Garcia, Z. and Bousso, P. (2005) CD4 T cells integrate signals delivered during successive DC encounters in vivo. J. Exp. Med. 202, 1271-1278.

Celli, S., Lemaitre, F. and Bousso, P. (2007) Real-time manipulation of T cell-dendritic cell interactions in vivo reveals the importance of prolonged contacts for CD4+ T cell activation. Immunity 27, 625-34.

Centonze, V.E. and White, J.G. (1998) Multiphoton Excitation Provides Optical Sections from Deeper within Scattering Specimens than Confocal Imaging. Biophys. J. 75, 2015-2024.

Chaigneau, E., Oheim, M., Audinat, E. and Charpak, S. (2003) Two-photon imaging of capillary blood flow in olfactory bulb glomeruli. PNAS 100, 13081-13086.

Christie, R.H., Bacskai, B.J., Zipfel, W.R., Williams, R.M., Kajdasz, S.T., Webb, W.W. and Hyman, B.T. (2001) Growth Arrest of Individual Senile Plaques in a Model of Alzheimer's Disease Observed by In Vivo Multiphoton Microscopy. J. Neurosci. 21, 858-864.

Corl, F.M., Garland, M.R., Lawler, L.P. and Fishman, E.K. (2002) A five-step approach to digital image manipulation for the radiologist. Radiographics 22, 981-92.

Denk, W., Piston, D.W. and Webb, R.H. (1995) Two-photon molecular excitation in laser scanning microscopy. In the Handbook of Confocal Microscopy, 445-458.

Denk, W., Strickler, J. and Webb, W. (1990) Two-photon Laser Scanning Fluorescence Microscopy. Science 248, 73-76.

Denk, W. and Svoboda, K. (1997) Photon Upmanship: Why Multiphoton Imaging is More that a Gimmick. Neuron 18, 351-357.

Di Rosa, F. and Santoni, A. (2002) Bone marrow CD8 T cells are in a different activation state than those in lymphoid periphery. Eur J Immunol 32, 1873-80.

Di Rosa, F. and Santoni, A. (2003) Memory T-cell competition for bone marrow seeding. Immunology 108, 296-304.

Diaspro, A., Federici, F. and Robello, M. (2002) Influence of refractive-index mismatch in high-resolution three-dimensional confocal microscopy. Applied Optics 41, 685-690.

Ellyard, J.I., Avery, D.T., Phan, T.G., Hare, N.J., Hodgkin, P.D. and Tangye, S.G. (2004) Antigen-selected, immunoglobulin-secreting cells persist in human spleen and bone marrow. Blood 103, 3805-12.

Feuerer, M., Beckhove, P., Garbi, N., Mahnke, Y., Limmer, A., Hommel, M., Hämmerling, G.J., Kyewski, B., Hamann, A., Umansky, V. and Schirrmacher, V. (2003) Bone marrow as a priming site for T-cell responses

to blood-borne antigen. Nat Med 9, 1151-1157.

Fischer, U., Jacovetty, E., Medeiros, R., Goudy, B., Zell, T., Swanson, J.-B., Lorenz, E., Shimizu, Y., Miller, M., Khoruts, A. and Ingulli, E. (2007) MHC class II deprivation impairs CD4 T cell motility and responsiveness to antigen-bearing dendritic cells in vivo. Proceedings of the National Academy of Sciences 104, 7181-7186.

Friedl, P., Wolf, K., Von Andrian, U.H. and Harms, G. (2007) Biological second and third harmonic generation microscopy. Curr Protoc Cell Biol. March, Unit 4.15.

Garaschuk, O., Milos, R., Grienberger, C., Marandi, N., Adelsberger, H. and Konnerth, A. (2006) Optical monitoring of brain function in vivo: from neurons to networks. Pflugers Arch 453, 385-96.

Garcia-Alloza, M., Borrelli, L., Rozkalne, A., Hyman, B. and Bacskai, B. (2007) Curcumin labels amyloid pathology in vivo, disrupts existing plaques, and partially restores distorted neurites in an Alzheimer mouse model. Journal of Neurochemistry 102, 1095-1104.

Garcia-Alloza, M., Dodwell, S., Meyer-Luehmann, M., Hyman, B. and Bacskai, B. (2006) Plaque-derived oxidative stress mediates distorted neurite trajectories in the Alzheimer mouse model. J Neuropathol Exp Neurol. 65, 1082-9.

Garrod, K., Wei, S., Parker, I. and Cahalan, M. (2007) Natural killer cells actively patrol peripheral lymph nodes forming stable conjugates to eliminate MHC-mismatched targets. Proceedings of the National Academy of Sciences 104, 12081-12086.

Germain, R.N. (2005) Imaging dynamic interactions in immune responses. Semin Immunol 17, 385-6.

Germain, R.N., Bajenoff, M., Castellino, F., Chieppa, M., Egen, J.G., Huang, A.Y., Ishii, M., Koo, L.Y. and Qi, H. (2008) Making friends in out-of-the-way places: how cells of the immune system get together and how they conduct their business as revealed by intravital imaging. Immunol Rev 221, 163-81.

Germain, R.N., Castellino, F., Chieppa, M., Egen, J.G., Huang, A.Y., Koo, L.Y. and Qi, H. (2005) An extended vision for dynamic high-resolution intravital immune imaging. Semin Immunol 17, 431-41.

Germain, R.N., Miller, M.J., Dustin, M.L. and Nussenzweig, M.C. (2006) Dynamic imaging of the immune system: progress, pitfalls and promise 6, 497-507.

Gobel, W. and Helmchen, F. (2007) New Angles on Neuronal Dendrites In Vivo. J Neurophysiol 98, 3770-3779.

Göppert-Mayer, M. (1931) Über Elementarakte mit zwei Quantensprüngen. Ann. Phys. 9, 273-295.

Grayson, M.H., Chaplin, D.D., Karl, I.E. and Hotchkiss, R.S. (2001) Confocal fluorescent intravital microscopy of the murine spleen. Journal of Immunological Methods 256, 55-63.

Grimaud, J., Lai, M., Thorpe, J., Adeleine, P., Wang, L., Barker, G.J., Plummer, D.L., Tofts, P.S., McDonald, W.I. and Miller, D.H. (1996) Quantification of

MRI lesion load in multiple sclerosis: A comparison of three computer-assisted techniques. Magnetic Resonance Imaging 14, 495-505.

Halin, C., Mora, J.R., Sumen, C. and Von Andrian, U.H. (2005) In Vivo Imaging of Lymphocyte Trafficking. Annu. Rev. Cell Dev. Biol. 21, 581-603.

Hallek, M., Bergsagel, P. and Anderson, K. (1998) Multiple myeloma: increasing evidence for a multistep transformation process. Blood 1, 3-21.

Harvey, C., Yasuda, R., Zhong, H. and Svoboda, K. (2008) The Spread of Ras Activity Triggered by Activation of a Single Dendritic Spine. Science 321, 136-140.

Harvey, C.D. and Svoboda, K. (2007) Locally dynamic synaptic learning rules in pyramidal neuron dendrites 450, 1195-1200.

Hauser, A., Junt, T., Mempel, T., Sneddon, M., Kleinstein, S., Henrickson, S., von Andrian, U., Shlomchik, M. and Haberman, A. (2007) Definition of germinal-center B cell migration in vivo reveals predominant intrazonal circulation patterns. Immunity 26, 655-67.

Hell, S., Reiner, G., Cremer, C. and Steltzer, E. (1993) Aberrations in confocal fluorescence microscopy induced by mismatches in refractive index. J Microsc 169, 391-405.

Helmchen, F. and Denk, W. (2002) New developments in multiphoton microscopy. Current Opinion in Neurobiology 12, 593-601.

Helmchen, F., Svoboda, K., Denk, W. and Tank, D.W. (1999) In vivo dendritic calcium dynamics in deep-layer cortical pyramidal neurons. Nat Neurosci 2, 989-996.

Henrickson, S., Mempel, T., Mazo, I., Liu, B., Artyomov, M., Zheng, H., Peixoto, A., Flynn, M., Senman, B., Junt, T., Wong, H., Chakraborty, A. and von Andrian, U. (2008a) In vivo imaging of T cell priming. Sci Signal. 1, pt2.

Henrickson, S.E., Mempel, T.R., Mazo, I.B., Liu, B., Artyomov, M.N., Zheng, H., Peixoto, A., Flynn, M.P., Senman, B., Junt, T., Wong, H.C., Chakraborty, A.K. and von Andrian, U.H. (2008b) T cell sensing of antigen dose governs interactive behavior with dendritic cells and sets a threshold for T cell activation 9, 282-291.

Hermans, M., Hartsuiker, H. and Opstelten, D. (1989) An in situ study of B-lymphocytopoiesis in rat bone marrow. Topographical arrangement of terminal deoxynucleotidyl transferase-positive cells and pre-B cells. J Immunol 142, 67-73.

Hoffmann, T.F., Leiderer, R., Waldner, H., Arbogast, S. and Messmer, K. (1995) Ischemia reperfusion of the pancreas: a new in vivo model for acute pancreatitis in rats. Res Exp Med (Berl) 195, 125-44.

Hopt, A. and Neher, E. (2001) Highly Nonlinear Photodamage in Two-Photon Fluorescence Microscopy. Biophys. J. 80, 2029-2036.

Horny, H., Engst, U., Walz, R. and Kaiserling, E. (1989) In situ immunophenotyping of lymphocytes in human bone marrow: an immunohistochemical study. Br J Haematol 71, 313-321.

Jacobsen, K. and Osmond, D. (1990) Microenvironmental Organization and Stromal Cell Associations of B Lymphocyte Precursor Cells in Mouse Bone Marrow. Eur J Immunol 20, 2395-2404.

Johnson, L., Walsh, M., Bockus, B. and Chen, L. (1981) Monitoring of relative mitochondrial membrane potential in living cells by fluorescence microscopy. J. Cell Biol. 88, 526-535.

Junt, T., Schulze, H., Chen, Z., Massberg, S., Goerge, T., Krueger, A., Wagner, D.D., Graf, T., Italiano, J.E., Jr., Shivdasani, R.A. and von Andrian, U.H. (2007) Dynamic Visualization of Thrombopoiesis Within Bone Marrow. Science 317, 1767-1770.

Kedrin, D., Wyckoff, J., Sahai, E., Condeelis, J. and Segall, J. (2007) Imaging tumor cell movement in vivo. Curr Protoc Cell Biol. 19.

Kim, D.-Y. and Park, J.-W. (2004) Computerized quantification of carotid artery stenosis using MRA axial images. Magnetic Resonance Imaging 22, 353-359.

Kinosita, R. and Ohno, S. (1960) Studies on bone marrow biodynamics: Observations on microcirculation in rabbit bone marrow in situ. Eur. Conf. Microcirc. 1, 106-109.

Kirkeby, S. and Thomsen, C.E. (2005) Quantitative immunohistochemistry of fluorescence labelled probes using low-cost software. J Immunol Methods 301, 102-13.

König, K. (2000) Multiphoton microscopy in life sciences. Journal of Microscopy 200, 83-104.

Kvasnicka, H., Thiele, J., Amend, T. and Fischer, R. (1994) Three-dimensional Reconstruction of Histologic Structures in Human Bone Marrow from Serial Sections of Threphine Biopsies. Analyt Quant Cytol Histol 16, 159-166.

Lai Guan Ng, P.M., Ichiko Kinjyo, Steven L. Reiner, Wolfgang Weninger,. (2008) Two-photon imaging of effector T-cell behavior: lessons from a tumor model. Immunological Reviews 221, 147-162.

Laudanna, C. and Constantin, G. (2003) New models of intravital microscopy for analysis of chemokine receptor-mediated leukocyte vascular recognition. Journal of Immunological Methods 273, 115-123.

Le Grand, Y., Leray, A., Guilbert, T. and Odin, C. (2008) Non-descanned versus descanned epifluorescence collection in two-photon microscopy: Experiments and Monte Carlo simulations. Optics Communications 281, 5480-5486.

Lehr, H.A., Mankoff, D.A., Corwin, D., Santeusanio, G. and Gown, A.M. (1997) Application of photoshop-based image analysis to quantification of hormone receptor expression in breast cancer. J Histochem Cytochem 45, 1559-65.

Lehr, H.A., van der Loos, C.M., Teeling, P. and Gown, A.M. (1999) Complete chromogen separation and analysis in double immunohistochemical stains using Photoshop-based image analysis. J Histochem Cytochem 47, 119-26.

Lendvai, B., Stern, E.A., Chen, B. and Svoboda, K. (2000) Experience-dependent plasticity of dendritic spines in the developing rat barrel cortex in vivo.

Nature 404, 876-881.

Leung, H. (1993) The Importance of Mounting Medium's Refractive Index and Cover Glass Thickness for Reducing Optical Aberration in a Confocal Laser Scanning Microscope (CLSM). Microscopical Society of Canada Bulletin 21, 19-24.

Leung, H. and Jeun, G. (1992) Errors in measurement induced by varying illumination, detector aperture diameter, and signal amplification in a confocal laser scanning microscope. Microscopical Society of Canada Bulletin 20, 26-33.

Lord, B., Testa, N. and Hendry, J. (1975) The relative spatial distributions of CFUs and CFUc in the normal mouse femur. Blood 46, 65-72.

Manjunath, N., Shankar, P., Wan, J., Weninger, W., Crowley, M.A., Hieshima, K., Springer, T.A., Fan, X., Shen, H., Lieberman, J. and von Andrian, U.H. (2001) Effector differentiation is not prerequisite for generation of memory cytotoxic T lymphocytes. J. Clin. Invest. 108, 871-878.

Manz, R.A., Thiel, A. and Radbruch, A. (1997) Lifetime of plasma cells in the bone marrow. Nature 388, 133-4.

Masters, B., So, P. and Gratton, E. (1998) Multiphoton Excitation Microscopy of In Vivo Human Skin: Functional and Morphological Optical Biopsy Based on Three-Dimensional Imaging, Lifetime Measurements and Fluorescence Spectroscopy. Ann of NY Academy of Sciences 838, 58-67.

Mazo, I., Honczarenko, M., Leung, H., Cavanagh, L., Bonasio, R., Weninger, W., Engelke, K., Xia, L., McEver, R., Koni, P., Silberstein, L. and von Andrian, U. (2005) Bone Marrow Is a Major Reservoir and Site of Recruitment for Central Memory CD8+ T Cells. Immunity 22, 259-270.

Mazo, I. and Von Andrian, U.H. (1999) Adhesion and homing of blood-borne cells in bone marrow microvessels. Journal of Leukocyte Biology 66, 25-32.

Mazo, I.B., Gutierrez-Ramos, J.-C., Frenette, P.S., Hynes, R.O., Wagner, D.D. and von Andrian, U.H. (1998) Hematopoietic Progenitor Cell Rolling in Bone Marrow Microvessels: Parallel Contributions by Endothelial Selectins and Vascular Cell Adhesion Molecule 1 J. Exp. Med. 188, 465-474.

Mazo, I.B., Quackenbush, E.J., Lowe, J.B. and von Andrian, U.H. (2002) Total body irradiation causes profound changes in endothelial traffic molecules for hematopoietic progenitor cell recruitment to bone marrow. Blood 99, 4182-4191.

McCuskey, R., McClugage, S. and Younker, W. (1971) Microscopy of living bone marrow in situ. Blood 38, 87-95.

Mempel, T.R., Henrickson, S.E. and Von Andrian, U.H. (2004a) T-cell priming by dendritic cells in lymph nodes occurs in three distinct phases. Nature 427, 154-9.

Mempel, T.R., Pittet, M.J., Khazaie, K., Weninger, W., Weissleder, R., von Boehmer, H. and von Andrian, U.H. (2006) Regulatory T cells reversibly suppress cytotoxic T cell function independent of effector differentiation. Immunity 25, 129-41.

Mempel, T.R., Scimone, M.L., Mora, J.R. and von Andrian, U.H. (2004b) In vivo imaging of leukocyte trafficking in blood vessels and tissues. Current Opinion in Immunology 16, 406-417.

Meyer-Luehmann, M., Spires-Jones, T.L., Prada, C., Garcia-Alloza, M., de Calignon, A., Rozkalne, A., Koenigsknecht-Talboo, J., Holtzman, D.M., Bacskai, B.J. and Hyman, B.T. (2008) Rapid appearance and local toxicity of amyloid-beta plaques in a mouse model of Alzheimer/'s disease 451, 720-724.

Miller, M., Hejazi, A., Wei, S., Cahalan, M. and Parker, I. (2004a) T cell repertoire scanning is promoted by dynamic dendritic cell behavior and random T cell motility in the lymph node. Proceedings of the National Academy of Sciences 101, 998-1003.

Miller, M., Safrina, O., Parker, I. and Cahalan, M. (2004b) Imaging the Single Cell Dynamics of CD4+ T Cell Activation by Dendritic Cells in Lymph Nodes. J. Exp. Med. 200, 847-856.

Miller, M.J., Wei, S.H., Cahalan, M.D. and Parker, I. (2003) Autonomous T cell trafficking examined in vivo with intravital two-photon microscopy. PNAS 100, 2604-2609.

Miller, M.J., Wei, S.H., Parker, I. and Cahalan, M.D. (2002) Two-Photon Imaging of Lymphocyte Motility and Antigen Response in Intact Lymph Node. Science 296, 1869-1873.

Miltenyi Biotec. (Auburn, CA) http://www.miltenyibiotec.com/.

Minski, M. (1961) Microscopy apparatus. In: US patent 3013467.

Mofidi, R., Walsh, R., Ridgway, P.F., Crotty, T., McDermott, E.W., Keaveny, T.V., Duffy, M.J., Hill, A.D. and O'Higgins, N. (2003) Objective measurement of breast cancer oestrogen receptor status through digital image analysis. Eur J Surg Oncol 29, 20-4.

Mora, J.R. and von Andrian, U.H. (2006) T-cell homing specificity and plasticity: new concepts and future challenges. Trends Immunol 27, 235-43.

Murphy, T., Li, P., Betts, K. and Liu, R. (2008) Two-Photon Imaging of Stroke Onset In Vivo Reveals That NMDA-Receptor Independent Ischemic Depolarization Is the Major Cause of Rapid Reversible Damage to Dendrites and Spines. J. Neurosci. 28, 1756-1772.

Naito, K., Tamahashi, N., Chiba, T., Kaneda, K., Okuda, M., Endo, K., Yoshinaga, K. and Takahashi, T. (1992) The Microvasculature of the Human Bone Marrow Correlated with the Distribution of Hematopoietic Cells. A Computer-Assisted Three-Dimensional Reconstruction Study. Tohoku J Exp Med 166, 439-450.

Nakamura, O. (1999) Fundamental of two-photon microscopy. Microscopy Research and Techniques 47, 165-171.

Neil, M.A., Juskaitis, R., Booth, M.J., Wilson, T., Tanaka, T. and Kawata, S. (2000) Adaptive aberration correction in a two-photon microscope. J Microsc 200 (Pt 2), 105-8.

Nilsson, S., Johnston, H. and Coverdale, J. (2001) Spatial localization of

transplanted hemopoietic stem cells: inferences for the localization of stem cell niches. Blood 97, 2293-9.

O'Shaughnessy, A.M. and Fitzgerald, D.E. (2000) Determining the stage of organisation and natural history of venous thrombosis using computer analysis. Int Angiol 19, 220-7.

Osmond, D. (1986) Population dynamics of bone marrow B lymphocytes. Immunlog. Rev. 93, 103-124.

Pannerale, L., Morini, S., D´ubaldo, E., Gaudio, E. and Marinozzi, G. (1997) SEM Corrosion-Casts Study of the Microcirculation of the Falt Bones in the Rat. The Anatomical Record 247, 462-471.

Paramithiotis, E. and Cooper, M.D. (1997) Memory B lymphocytes migrate to bone marrow in humans. Proc Natl Acad Sci U S A 94, 208-12.

Patterson, G.H. and Piston, D.W. (2000) Photobleaching in two-photon excitation microscopy. Biophys J 78, 2159-62.

Patton, P., Jokisch, D., Rajon, D., Shah, A., Myers, S., Inglis, B. and Bolch, W. (2002) Skeletal dosimetry via NMR Microscopy: Investigations of sample reproducibility and signal source. Health Physics 82, 316-326.

Piccio, L., Rossi, B., Scarpini, E., Laudanna, C., Giagulli, C., Issekutz, A.C., Vestweber, D., Butcher, E.C. and Constantin, G. (2002) Molecular mechanisms involved in lymphocyte recruitment in inflamed brain microvessels: critical roles for P-selectin glycoprotein ligand-1 and heterotrimeric G(i)-linked receptors. J Immunol 168, 1940-9.

Pothuaud, L., Laib, A., Levitz, P., Benhamou, C.L. and Majumdar, S. (2002) Three-dimensional-line skeleton graph analysis of high-resolution magnetic resonance images: a validation study from 34-microm-resolution microcomputed tomography. J Bone Miner Res 17, 1883-95.

Prada, C., Garcia-Alloza, M., Betensky, R., Zhang-Nunes, S., Greenberg, S., Bacskai, B. and Frosch, M. (2007) Antibody-Mediated Clearance of Amyloid-{beta} Peptide from Cerebral Amyloid Angiopathy Revealed by Quantitative In Vivo Imaging. J. Neurosci. 27, 1973-1980.

Rajewsky, K. (1996) Clonal selection and learning in the antibody system 381, 751-758.

Ranefall, P., Wester, K., Busch, C., Malmstrom, P.U. and Bengtsson, E. (1998) Automatic quantification of microvessels using unsupervised image analysis. Anal Cell Pathol 17, 83-92.

Rosenbaum, J.T., Planck, S.R., Martin, T.M., Crane, I., Xu, H. and Forrester, J.V. (2002) Imaging ocular immune responses by intravital microscopy. Int Rev Immunol 21, 255-72.

Schirrmacher, V., Feuerer, M., Fournier, P., Ahlert, T., Umansky, V. and Beckhove, P. (2003) T-cell priming in bone marrow: the potential for long-lasting protective anti-tumor immunity. Trends Mol Med 9, 526-34.

Schnapper, A., Reumann, K. and Meyer, W. (2002) The architecture of growing compact bone in the dog: visualization by 3D-reconstruction of histological sections. Ann Anat 184, 229-233.

Sheppard, C. and Torok, P. (1997) Effects of specimen refractive index on confocal imaging. J Microsc 185, 366-374.

Sherman, L., Ye, J.Y., Albert, O. and Norris, T.B. (2002) Adaptive correction of depth-induced aberrations in multiphoton scanning microscopy using a deformable mirror. J Microsc 206, 65-71.

Sikora, L., Johansson, A.C., Rao, S.P., Hughes, G.K., Broide, D.H. and Sriramarao, P. (2003) A murine model to study leukocyte rolling and intravascular trafficking in lung microvessels. Am J Pathol 162, 2019-28.

Slifka, M., Antia, R., Whitmire, J. and Ahmed, R. (1998) Humoral immunity due to long-lived plasma cells. Immunity 8, 363-72.

Smedegard, G., Bjork, J. and Arfors, K.E. (1985) An intravital microscopy model for studies of immune complex induced inflammation at the microvascular level. Int J Tissue React 7, 55-60.

Squirrell, J.M., Wokosin, D.L., White, J.G. and Bavister, B.D. (1999) Long-term two-photon fluorescence imaging of mammalian embryos without compromising viability. Nat Biotechnol 17, 763-7.

Sugawara, Y., Kamioka, H., Honjo, T., Tezuka, K. and Takano-Yamamoto, T. (2005) Three-dimensional reconstruction of chick calvarial osteocytes and their cell processes using confocal microscopy. Bone 36, 877-83.

Sumen, C., Mempel, T.R., Mazo, I.B. and von Andrian, U.H. (2004) Intravital Microscopy: Visualizing Immunity in Context. Immunity 21, 315-329.

Svoboda, K., Denk, W., Kleinfeld, D. and Tank, D.W. (1997) In vivo dendritic calcium dynamics in neocortical pyramidal neurons. [Letter]. Nature 385, 161-165.

Tokoyoda, K., Egawa, T., Sugiyama, T., Choi, B. and Nagasawa, T. (2004) Cellular Niches Controlling B Lymphocyte Behavior within Bone Marrow during Development. Immunity 20, 707-718.

Tozer, G.M., Ameer-Beg, S.M., Baker, J., Barber, P.R., Hill, S.A., Hodgkiss, R.J., Locke, R., Prise, V.E., Wilson, I. and Vojnovic, B. (2005) Intravital imaging of tumour vascular networks using multi-photon fluorescence microscopy. Adv Drug Deliv Rev 57, 135-52.

Tripp, R., Topham, D., Watson, S. and Doherty, P. (1997) Bone marrow can function as a lymphoid organ during a primary immune response under conditions of disrupted lymphocyte trafficking. J Immunol 158, 3716-20.

Tyrrell, J.A., Mahadevan, V., Tong, R.T., Brown, E.B., Jain, R.K. and Roysam, B. (2005) A 2-D/3-D model-based method to quantify the complexity of microvasculature imaged by in vivo multiphoton microscopy. Microvasc Res 70, 165-78.

Umesh Adiga, P.S. and Chaudhuri, B.B. (2001) Some efficient methods to correct confocal images for easy interpretation. Micron 32, 363-70.

Vilaplana, J. and Lavialle, M. (1999) A method to quantify glial fibrillary acidic protein immunoreactivity on the suprachiasmatic nucleus. J Neurosci Methods 88, 181-7.

von Andrian, U.H. (1996) Intravital microscopy of the peripheral lymph node microcirculation in mice. Microcirculation 3, 287-300.

Wang, W., Wyckoff, J., Goswami, S., Wang, Y., Sidani, M., Segall, J. and Condeelis, J. (2007) Coordinated Regulation of Pathways for Enhanced Cell Motility and Chemotaxis Is Conserved in Rat and Mouse Mammary Tumors. Cancer Res 67, 3505-3511.

Warnock, R.A., Askari, S., Butcher, E.C. and Andrian, U.H.v. (1998) Molecular Mechanisms of Lymphocyte Homing to Peripheral Lymph Nodes. J. Exp. Med. 187, 205-216.

Wearne, S.L., Rodriguez, A., Ehlenberger, D.B., Rocher, A.B., Henderson, S.C. and Hof, P.R. (2005) New techniques for imaging, digitization and analysis of three-dimensional neural morphology on multiple scales. Neuroscience 136, 661-80.

Wei, S., Parker, I., Miller, M. and Cahalan, M. (2003) A stochastic view of lymphocyte motility and trafficking within the lymph node. Immunological Reviews 195, 136-159.

Weiss, L. (1965) The structure of bone marrow. Functional interrelationships of vascular and hematopoietic compartements in experimental hemolytic anemia: an electron microscopic study. J Morphol. 117, 467-537.

Weninger, W., Crowley, M.A., Manjunath, N. and Von Andrian, U.H. (2001) Migratory Properties of Naive, Effector, and Memory CD8+ T Cells. J Exp Med 194, 953-966.

Wolf, K., Mazo, I., Leung, H., Engelke, K., von Andrian, U.H., Deryugina, E.I., Strongin, A.Y., Brocker, E.-B. and Friedl, P. (2003) Compensation mechanism in tumor cell migration: mesenchymal-amoeboid transition after blocking of pericellular proteolysis. J. Cell Biol. 160, 267-277.

Worbs, T., Mempel, T.R., Bolter, J., von Andrian, U.H. and Forster, R. (2007) CCR7 ligands stimulate the intranodal motility of T lymphocytes in vivo. J. Exp. Med. 204, 489-495.

Xu, C. and Webb, W. (1996) Measurement of two-photon excitation cross sections of molecular florophores with data from 690 to 990 nm. J. Opt. Soc. Am. B 13, 481-491.

Xu, C., Zipfel, W., Shear, J.B., Williams, R.M. and Webb, W.W. (1996) Multiphoton fluorescence excitation: New spectral windows for biological nonlinear microscopy. PNAS 93, 10763-10768.

Yoder, E. and Kleinfeld, D. (2002) Cortical Imaging Through the Intact Mouse Skull Using Two-Photon Excitation Laser Scanning Microscopy. Microscopy Research and Techniques 56, 304-305.

Zhang, J., Niu, C., Ye, L., Huang, H., He, X., Tong, W., Ross, J., Haug, J., Johnson, T., Feng, J., Harris, S., Wiedemann, L., Mishina, Y. and Li, L. (2003) Identification of the haematopoietic stem cell niche and control of the niche size. Nature 425, 836-841.

Zinselmeyer, B., Lynch, J., Zhang, X., Aoshi, T. and Miller, M. (2008) Video-rate two-photon imaging of mouse footpad - a promising model for studying

leukocyte recruitment dynamics during inflammation. Inflamm Res. 57, 93-6.

Zipfel, W.R., Williams, R.M., Christie, R., Nikitin, A.Y., Hyman, B.T. and Webb, W.W. (2003) Live tissue intrinsic emission microscopy using multiphoton-excited native fluorescence and second harmonic generation. Proc Natl Acad Sci U S A 100, 7075-80.

9 Danksagung

Ich bedanke mich bei Herrn Prof. Dr. Fritz Krombach für die persönliche Unterstützung bei der Verfassung dieser Arbeit sowie die Möglichkeit der Promotion am Walter-Brendel-Zentrum für Experimentelle Medizin in München.

Bei Herrn Prof. Dr. Ulrich von Andrian bedanke ich mich für die persönliche Unterstützung sowie die Möglichkeit, in der engagierten und freundlichen Atmosphäre seiner Abteilung in Boston zu forschen, ebenso für die kontinuierliche Betreuung während meines Forschungsaufenthalts und die hervorragende Anleitung zum wissenschaftlichen Arbeiten.

Herzlich danken möchte ich den Mitarbeitern in Boston, Harry Leung, Ira Mazo und Lucila Scimone für die methodische Anleitung, gute Zusammenarbeit und Unterstützung im Allgemeinen.

Darüber hinaus möchte ich meinen Eltern herzlichst danken für die liebevolle Unterstützung und Beratung während der gesamten Ausbildung, beim Verfassen dieser Arbeit, sowie auf meinem beruflichen Weg.

10 Curriculum Vitae

Persönliche Daten

Name	Katharina Engelke
Geboren am	15. April 1979 in Göttingen
Nationalität	Deutsch

Berufliche Tätigkeit

Seit 2008	Klinik und Poliklinik für Hals-Nasen-Ohrenheilkunde, Klinikum Großhadern, LMU, München: Assistenzärztin
2007	McKinsey & Company: Beratertätigkeit im „Healthcare“-Sektor

Hochschulausbildung

1998-2006	Studium der Humanmedizin an der Ludwigs-Maximilians-Universität München, Abschluss mit Note 1,7
2005-2006	Praktisches Jahr:
	Chirurgie im Hospital Fernandez, Universidad de Buenos Aires, Argentinien
	Innere Medizin in Mount Sinai School of Medicine, New York, NY, USA
	Anästhesie im Klinikum Großhadern, LMU, München
2003	„USMLE 1“ (United States Medical Licensing Examination)
2001-2002	Forschungsaufenthalt am IDI Immune Disease Institute, Harvard Medical School, Boston, MA, USA

Schulbildung

1991-1998	Theodor-Heuss-Gymnasium, Göttingen, Abitur mit Note 1,9
1995	Auslandsaufenthalt: Juanita High School, Kirkland, Seattle, WA, USA
1989-1991	Orientierungsstufe Lutherschule, Göttingen
1985-1989	Grundschule Höltyschule, Göttingen